Paragenesis, mineral chemical and microtextural studies of uranium bearing minerals in the brecciated albitites U-ores from the Kitongo shear zone, Poli region, northern Cameroon

Arnaud Patrice Kouske, Martine Gerard, Jacques Etame, Ngouo Sylvestre Kanouo, Milan Stafford Tchouatcha, Tanwi Richard Ghogomu, Michel Cuney, Suh Emmanuel Cheo, Vincent Ngako

Paragenesis, mineral chemical and microtextural studies of uranium bearing minerals in the brecciated albitites U-ores from the Kitongo shear zone, Poli region, northern Cameroon

Arnaud Patrice Kouske[1] · Martine Gerard[2] · Jacques Etame[3] · Ngouo Sylvestre Kanouo[4] · Milan Stafford Tchouatcha[5] · Tanwi Richard Ghogomu[6] · Michel Cuney[7] · Suh Emmanuel Cheo[8] · Vincent Ngako[9]

Abstract

The Kitongo uranium deposit is located in the northwestern margin of the post-tectonic alkaline batholith of Kogué emplaced at ca. 550–530 Ma. The hydrothermal alteration system that affected the Kitongo granite is manifested by two albitization events characterized by the development of aegirine–albitites (Na-metasomatites). These albitization events that occurred respectively as pre-ore and ore stages were continuous, spacially bound one another and were accompanied by calcitization (Ca-metasomatites) and hematitization of various intensity. Tectonic breccias that were formed during the reactivation of wrench faults represent the most prevelent U-ore morphology types developed along the Kitongo shear zone (KSZ). These breccias were investigated for their mineral paragenesis, mineral chemical and microtextural features of uranium bearing phases. The results reveal that U-ore phases are spherical with a mineral nucleus, massive aggregates or in veinlets with some of these U-minerals showing areas of various brightness suggesting a heterogeneous composition of U-mineral phases. Radiation damage aureoles develop around idiomorphic uraninite crystals as a result of alpha radiations on the enclosing magnetite. The gangue minerals consist of albite, riebeckite, aegirine, amphibole, monazite, magnetite, calcite, zircon, epidote, apatite and titanite. U-ore phases are heterogeneous and represent complex U-ore mineral assemblage in which both primary and secondary uranium phases were observed. Uraninite, the primary uranium mineral occurred in the form of isolated euhedral to subhedral grains. It showed low SiO_2, CaO, FeO, P_2O_5, ZrO_2, ThO_2 and Al_2O_3. The low ThO_2 content in this uraninite grains indicated that U-primary mineralization formed at a relatively low temperature. Uraninite grains were progressively converted to coffinite. This progressive conversion was manifested by the occurrence of coffinitised U-phase. Coffinite occurred both as replacement or vein type U-phase however with no apparent chemical difference. The other U-phases include U–Zr–Si, U–Fe–Si and U–Ti. Overall, the physical and geochemical characteristics of the U-bearing phases in the studied breccias suggest alternating oxidizing and reducing conditions during the formation of uranium ore that occurred during the second albitization phase along the KSZ.

Keywords Kitongo · Albitization · Breccias · Uranium deposit · U-ore phases

Introduction

Uranium can concentrate in about 200 mineral species (Burns and Finch 1999). A restricted number of these U-bearing minerals may occur in significant concentrations under specific geological conditions to form an ore deposit (Frondel and Fleischer 1955; Frondel 1958; Dahlkamp 1993; Finch and Murakami 1999; Edwards and Oliver 2000; Pownceby and Johnson 2013). Uranium ore deposits are extremely diversified and their metallogeny is directly related to the conditions under which they formed (Cuney 2009). Na-metasomatism is a widespread fluid-rock interaction where potassium and calcium are replaced by sodium (Cinelu and Cuney 2006; Cuney 2009; Alexandre 2010; Cuney et al. 2012; Kouske et al. 2012; Kouske 2013; Verissimo et al. 2016). This phenomenon is commonly accompanied by dequartzification, hematitization, Ca– and Fe–Na mineral new formation, chloritization and fluoritization (Abd El-Naby and Dawood 2008; Andreeva et al. 2010).

✉ Arnaud Patrice Kouske
arnaudpatricek@gmail.com

Extended author information available on the last page of the article

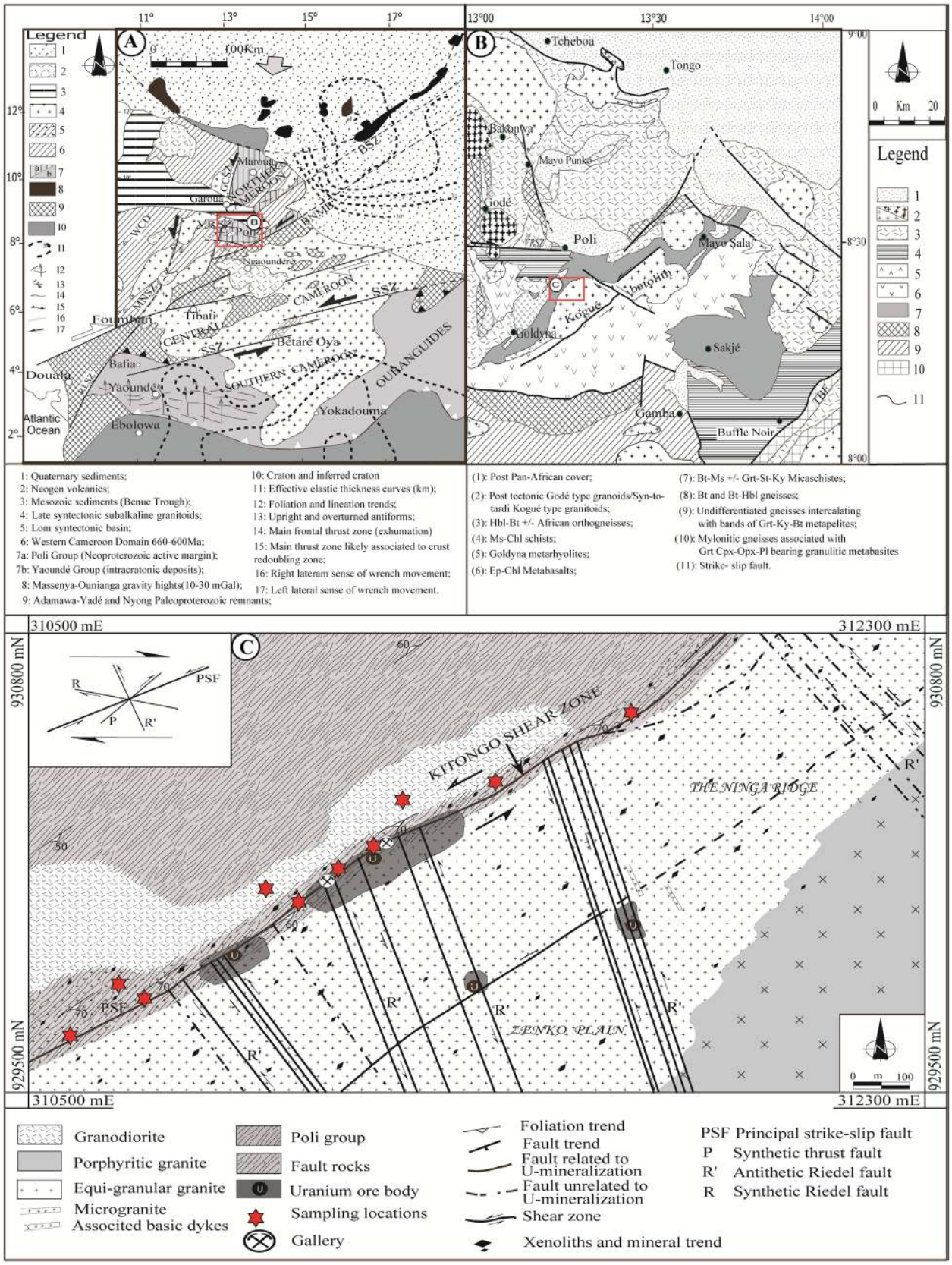
A
B
C
Legend
100Km
Tcheboa
Tongo
Bakontwa
Mayo Punko
Godé
Poli
Mayo Sala
Goldyna
Sakjé
Gamba
Buffle Noir
Foumban
Tibati
Bafia
Douala
Yaoundé
Ebolowa
Yokadouma
Atlantic Ocean
CAMEROON
SSZ
Bétaré Oya
SOUTHERN CAMEROON
OUBANGUIDES
CENTRAL
NORTHERN CAMEROON
BNMM
BSZ
WCD
MINSZ
TBF
TRZ
Ngaoundéré
Garoua
Maroua
Poli
Mayo Sala
Kogué
Toubouri
0 Km 20
1: Quaternary sediments;
2: Neogen volcanics;
3: Mesozoic sediments (Benue Trough);
4: Late syntectonic subalkaline granitoids;
5: Lom syntectonic basin;
6: Western Cameroon Domain 660-600Ma;
7a: Poli Group (Neoproterozoic active margin);
7b: Yaoundé Group (intracratonic deposits);
8: Massenya-Ounianga gravity hights(10-30 mGal);
9: Adamawa-Yadé and Nyong Paleoproterozoic remnants;
10: Craton and inferred craton
11: Effective elastic thickness curves (km);
12: Foliation and lineation trends;
13: Upright and overturned antiforms;
14: Main frontal thrust zone (exhumation)
15: Main thrust zone likely associated to crust redoubling zone;
16: Right lateram sense of wrench movement;
17: Left lateral sense of wrench movement.
(1): Post Pan-African cover;
(2): Post tectonic Godé type granoids/Syn-to-tardi Kogué type granitoids;
(3): Hbl-Bt +/- African orthogneisses;
(4): Ms-Chl schists;
(5): Goldyna metarhyolites;
(6): Ep-Chl Metabasalts;
(7): Bt-Ms +/- Grt-St-Ky Micaschistes;
(8): Bt and Bt-Hbl gneisses;
(9): Undifferentiated gneisses intercalating with bands of Grt-Ky-Bt metapelites;
(10): Mylonitic gneisses associated with Grt Cpx-Opx-Pl bearing granulitic metabasites
(11): Strike- slip fault.
310500 mE
312300 mE
930800 mN
929500 mN
KITONGO SHEAR ZONE
THE NINGA RIDGE
ZENKO PLAIN
PSF
R
R'
P
0 m 100
Granodiorite
Porphyritic granite
Equi-granular granite
Microgranite
Associted basic dykes
Poli group
Fault rocks
Uranium ore body
Sampling locations
Gallery
Foliation trend
Fault trend
Fault related to U-mineralization
Fault unrelated to U-mineralization
Shear zone
Xenoliths and mineral trend
PSF Principal strike-slip fault
P Synthetic thrust fault
R' Antithetic Riedel fault
R Synthetic Riedel fault

◂**Fig. 1** The location maps indicating successively (**A**) the structural map of the eastern province of the CAFB (modified from Ngako et al 2008), (**B**) Geological map of the Poli region, modified from Toteu et al. (2006), (**C**) Geological map of the Kitongo uranium deposit (modified from Kouske et al. 2012)

The aforementioned phenomena can be associated with the incorporation of specific trace elements into the crystallizing uranium minerals. The composition and temperature of the mineralizing fluids highly influence the nature and the quantity of the incorporated elements (Janeczek and Ewing 1992a). However, the composition of crystallized uranium minerals is frequently modified by post-depositional re-equilibration with later fluids under variable physical–chemical conditions (Alexandre and Kyser 2005). This is the case of the infiltration of meteoric waters through the secondary rock porosity which commonly leads to the oxidation of primary uranium (U^{4+}) into "secondary" hexavalent (U^{6+}) uranyl minerals (Finch and Murakami 1999).

Previous works revealed that the Kitongo area has witnessed at least two phases of albitization which could be related to the Paleozoic–Mesozoic volcanism and Tertiary syenitic ring complex over the Poli area (Oesterlen and Vetter 1986). Recently, Kouske et al. (2012) and Kouske (2013) presented structural data for the Kitongo U- deposit and whole-rock geochemical composition of the host- rocks and these authors suggested that U-related sodium metasomatism at Kitongo is structurally controlled (Fig. 1c). This mineralization is found in three morphology types including the massive ore bodies (of limited extension), fault zone and breccias. Fault zone occurring along the Kitongo shear zone (KSZ) are constituted by the intercalations of the Kitongo granite and Poli Group (Kouske et al. 2012). Breccias mostly occur at fault intersections between the KSZ and the conjugate Riedel R' shears types. Despite the aforementioned works, the genesis of the U-ore bodies is not well constrained; information characterizing ore minerals found in the mineralization are still not available and the source of uranium remains poorly evaluated. Thus, the objective of this paper is to contribute to a better understanding of the processes surrounding the genesis of the Kitongo uranium deposit.

Geological setting

The Kitongo uranium deposit lies in the northwestern part of the Kitongo granitoid along the ENE-WSW trending KSZ (Fig. 1). This granitoid is found as an intrusion within the Poli Group located in the northern part of the Central African Fold Belt (CAFB). The aforementioned Group represents an early Neoproterozoic back-arc basin formed between 830 and 665 Ma (Toteu 1990; Toteu et al. 2001; Penaye et al. 2006). It is composed of many rock types: (1) detrital and volcanoclastic rocks (sandstones, shales, and conglomerates); (2) metavolcanic rocks (tholeiitic basalts and calc–alkaline rhyolites); (3) metasediments (schists, and gneisses); and (4) pre-, syn- to post-tectonic calc-alkaline intrusions among which diorites, granodiorites and granites (e.g. Le Fur 1971; Toteu et al. 1984; Njel 1986; Bassahak 1988; Penaye 1988; Toteu 1990; Pinna et al. 1994; Kouske et al. 2012; Kouske 2013). The post-tectonic calc-alkaline granitoids in the northern part of the CAFB among which the Kitongo granite were emplaced between 660 and 580 Ma and cross-cut Mesoproterozic to Neoproterozoic schists and gneisses (Toteu et al. 1987). The tectonic of this Group is marked by E–W antiform and synform characterizing gentle folding of a regional flat-lying foliation probably formed during an early thrust evolution (Ngako 1999; Ngako et al. 2008; Ngako and Njonfang 2011). Many generations of wrench zones in this area crosscut the early folds and foliation related to the thrusting and nappe refolding (Ngako et al. 2008; Ngako and Njonfang 2011). These include the left and right wrench movements: the D2 and D3 Pan-African phases involving major sinistral and dextral SZ that have almost operated at right angle.

Four main lithodemic units are distinguished at Kitongo (Kouske et al. 2012; Kouske 2013). These rocks representing the primary lithology in the Kitongo area are composed from the West to the East by: (1) Poli Group; (2) granodioritic unit; (3) fault zone; and (4) granitic unit (Fig. 1c). The Poli Group, cropping out in the northwest of Kitongo granitic unit, is mainly made up of interleaved dark-grey basic meta-volcanic and light-grey meta-sedimentary rocks, and amphibole-bearing schist with a strong N045-078E-trending regional foliation (Kouske et al. 2012; Kouske 2013). This unit is cross-cut by many faults and fractures with different strikes and dips (Kouske et al. 2012). The granodioritic unit is made up of older granodiorite xenoliths found in a younger granodiorite pluton (Kouske et al. 2012). The fault zone outcropping between the Kitongo granitic and granodioritic units is characterized by intercalations of rocks of the Poli Group and Kitongo granite. These intercalations exhibit a trellis aspect defining a sinistral shear zone averaging ~ 70 m wide with visible highly to weakly albitized mylonitic foliations (Kouske et al. 2012; Kouske 2013).The granitic unit (cut by mafic dykes) is texturally composed of porphyritic granite, equigranular granite and microgranite with the same mineralogical composition (Kouske et al. 2012; Kouske 2013). The margin of the Kitongo granite is affected by both ductile and brittle deformations. The ductile deformation is underlined by pervasive mineral lineation and linear fabrics (trending N050-066E, $\geq 65^{\circ}$SE) defined by xenoliths of micro-granodioritic composition. The brittle deformation is marked by a conjugate fault system (R'shears) and joints variably oriented that overprint the

Kitongo shear zone. The interplay between the KSZ and the aforementioned R'shears system yielded breccias. The development of the ductile to brittle deformation along the KSZ has favored fluid circulation that enabled the development of sodium metasomatism and uranium deposition.

Materials and methods

The studied samples were collected from the brecciated U-bearing albitites outcropping along the Kitongo shear zone (described in Kouske et al. 2012, Fig. 1c). Polished thin sections were prepared in Novosibirsk, Russia at the Department of Mineralogy CERCAMS (Centre for Russian and Central EurAsian Mineral Studies).Textural and mineralogical analyses were performed using optical microscope (at the Laboratory of Metallogeny of the University of Yaounde I, Cameroon) and backscattered electron (at the ECCE TERRA, OSU, Sorbonne University, France). Mineral assemblage, opaque minerals and uranium mineral phases were determined using Zeiss supra 55VP scanning electron microscope (SEM). Micro-morphological observations and mapping of polished thin sections were coupled with Wavelength Dispersive Spectrometry (WDS) analysis using microprobe Oxford Instrument INCA Energy 350XMax), conducted at 15 keV with a 450 pA probe current (at the Sorbonne University, France). The analysis accuracy was checked against standards such as albr, mnti, Fe_2o_3, ortr, phn9, ZrSi, mona, apat UO_2, Fes_2 respectively for Na (Kα),; Ti (Kα)-Mn (Kα); Fe (Kα); Al (Kα)-K (Kα); Mg (Kα) –Si (Kα) –Ca (Kα); Zr (Lα); Ce (Lα)-Th (Mα); P (Kα); U (Mα), and S (Kα) X-ray lines.

Results

Petrographic features of lithodemic units from the Kitongo area

The aforementioned geological setting has shown that in the Kitongo area, granodiorite and granite intruded the Poli Group and these two intrusion types are separated by fault zone underlining the ENE-WSW trending KSZ trace (Fig. 1c). In addition mafic dykes crosscut the Kitongo granite. Petrography of these lithodemic units are here after presented.

Granodiorite

This rock shows a dark to dark green color with the predominance of mafic minerals and a dominant coarse grained texture. The mineralogy is principally composed of plagioclase, quartz, alkali feldspar, amphibole (hornblende), biotite and pyroxene (Fig. 2a, b). Plagioclase, the most abundant feldspar shows a weakly to strongly developed polysynthetic twining. Sericitization develops mostly in the core of weakly twinned plagioclase grains. Quartz may occur as mono- or polycrystalline mineral. Alkali feldspar occurs as interstitial anhedral crystals. Hornblende represents the most abundant mafic phase of the bulk rock. Some flakes of this mineral show a dark green color with euhedral to anhedral shapes. Other hornblende flakes of green color may show basal sections with diamond-shaped cleavage (about 46°) in which titanite minerals may be included (Fig. 2a). Some other hornblende minerals may show a well-developed twinning (Fig. 2b). Biotite occurs essentially as flakes of various sizes and color (yellow brown to dark brown) and pleochroic. Pyroxene crystals show a yellowish color and shows straight extinction, its basal section presents cleavage at 87° (Fig. 2b). Besides the aforementioned titanite minerals, the other accessory minerals are apatite, zircon and opaque minerals; these mineral phases occur as free crystals or as inclusions in other mineral phases.

Fault zone

This lithodemic unit exhibits a treillis aspect characterized by intercalation of both Poli Group and granite. Microscopic observations of this fault zone revealed a mylonitic texture underlined by a strong schistosity (Fig. 2c). The mineralogical set is mainly composed of deformed quartz, feldspar and amphiboles crystals.

Mafic dykes

Two mafic dyke types were observed cutting across the Kitongo granitoid. They include micro-gabbroic and lamprophyric dykes (Kouske et al. 2012). Micro-gabbroic dykes are melanocratic, massive and very hard. This rock shows a dominant doleritic texture with oblong plagioclase crystals, associated with considerable amount of mafic minerals. The texture of these micro-gabbro dykes may become porphyritic with the occurrence of plagioclase, olivine and pyroxene phenocrysts (0.5–2 cm; Fig. 2d, e). Accessory minerals include opaque phases (that occur mostly as cubic crystals with various sizes), apatite and amphibole. Besides the cliff face, lamprophyric dykes are also observed on top of the Kitongo (Zenko plain, Fig. 1c). These dykes are greyish in color, dense and fine-grained and often broken into polyhedral blocks. The mineralogy of this rock is composed of large mineral phases such as plagioclase, clinopyroxene (Cpx) and calcite which, associated with opaque phases (Fig. 2f, g). Plagioclase crystals are typically lath-shaped and exhibit polysynthetic and simple twinning. Clinopyroxene phenocrysts show subhedral to anhedral shapes and are evenly distributed; however these minerals may form

clusters. Cpx in these rocks show various degree of alteration resulting in the formation calcite especially along the fractures (Fig. 2f). Some calcite minerals may completely replace pyroxene. In addition, some fractures and cleavage planes in the resulting calcite crystals are stained by reddish hematite (Fig. 2g).

Granite

Three facies are observed in the Kitongo granite: the microgranite, porphyritic granite and equigranular facies. Microgranite outcrops as dykes of pink color with limited extension (Fig. 1c). The texture of this rock is either mosaic or porphyritic micro-grained and both sub-facies show about the same mineralogical composition where quartz (30–40%) and feldspar (60–70%) are the dominant mineral phases. In the porphyritic micro-grained sub-facies, phenocryst phase (1–2 cm) is represented by subhedral to anhedral plagioclase and orthoclase minerals within a matrix of medium-grain size (2–3 mm) made up of K-feldspar (25–35%), plagioclase (20–30%), quartz (25–35%), amphibole (5%) and biotite (2%). Conversely, the equigranitic facies appears well crystallized with mineralogical assemblage close to that of the porphyritic granite. The average mineral grain size in this rock facies is 2 mm. Quartz crystals (Fig. 2p) may display amoeboid or polygonal shapes with undulose extinction. Plagioclase in this rock is subhedral to euhedral (Fig. 2i, j) and some crystals are locally zoned. Some plagioclase crystals are partially altered into sericite (Fig. 2j). Bent spindle plagioclase highlighting a plastic deformation can also be observed (Fig. 2p). K-feldspar is represented by orthoclase. This mineral occurs as subhedral to anhedral crystals showing simple Carlsbad twinning, vein perthite intergrowths (Fig. 2n) or cloudy aspect (Fig. 2p). Amphibole (hornblende) minerals are pale brown in color with some crystals appearing as zoned or unzoned euhedral phenocrysts (> 500 μm), tabular or prismatic microcrysts, or acicular microlites in groundmass (Fig. 2h, j, k, l, o). Some other amphibole crystals are green to brown color showing euhedral basal section displaying clivages or simple twinning (Fig. 2i), pleochroism and/or concentric zoning. Biotite crystals appear as isolated laths or polycrystalline lens-shaped aggregates. The Kitongo granite displays remarkable perthitic, granophyric, and mymekitic textures (Fig. 2m, n). Parsons and Lee (2009) interpreted such textures as coeval crystallization of quartz-feldspar, exsolution within feldspar, and dissolution–precipitation in the presence of a fluid under a temperature comprised between 450 and 550 °C. Monazite grains occur as anhedral grains enclosed in amphibole and some of them show radiohalos (Fig. 2k). Zircons are found enclosed in other mineral phases. These zircons are mostly euhedral grains with prismatic shape and bipyramidal terminations. Some of these zircon crystals display radiohalos as well (Fig. 2l). Titanite occurs as subhedral crystals exhibiting clivage planes with a pale brown color and surrounded by amphiboles and plagioclase (Fig. 2j). Apatite occurs as interstitial anhedral crystals or may be found included in ferromagnesian or feldspar minerals. Opaque phases occur as irregular aggregates, tiny inclusions or scattered flakes in mineral matrix. In addition to all these mineral phases, unidentified microcrystals displaying radiohalos around them are found as dispersed micro-inclusions in amphibole crystals (Fig. 2o).

Brecciated U-ore bodies

Brecciated uranium ore bodies along the KSZ show reddish coloration and are cross-cut by yellow veinlets (Fig. 3a). This reddish coloration is due to prominent Na-metasomatism. Their physical attributes enabled to discriminate them as tectonic breccias that were later on classified as clast-supported breccias based on the modal amount (75–90%). Clasts in these materials are mostly angular (Fig. 3c) and minor displacements are observed (Fig. 3d). Auto-brecciation texture is also commonly observed therein. This phenomenon is marked by incipient grain size reduction grading to cataclastic texture (Fig. 3b). In the tectonic breccias, the formation of hematite and carbonate contributed to consolidate the rock matrix.

Mineralogical features

The mineralogy in these breccias is dominantly composed of albite in association with variable amount of aegirine, riebeckite, magnetite, hematite, apatite, zircon and calcite (Table 1; Fig. 3d–j). Two generations of albite were identified: albite-1 (Ab1) that may occur as incipient transformation of K-feldspar (Fig. 3e) up to a total pseudomorphosic replacement of K-feldspar megacrysts. Some albite-1 crystals where crosscut by sub-parallel fractures with micro shearing in response to brittle deformation (Fig. 3d). Albite-2 (Ab2) crystallized in the porosity (vugs resulting from quartz dissolution and in micro-fractures) of the ore bodies. It is noteworthy that apart from albite crystals whose generations where discriminated by the relative chronology, the generations of the other mineral phases were difficult to establish due to the brecciation process (sometimes reaching mylonite texture) and the intensity of alteration in the studied breccias. Aegirine, green needle-like or red microcrystals occurs together with riebeckite (dark–light blue and massive-zoned to acicular) as a progressive replacement of amphibole crystals in breccias (Fig. 3g, h). Zoned riebeckite is shown in Fig. 4. Magnetite shows euhedral to anhedral shapes and is found in important quantity in the U-ore bodies, almost always close to aegirine and riebeckite (Figs. 3g, 5d, e and g). Magnetite may be interpreted

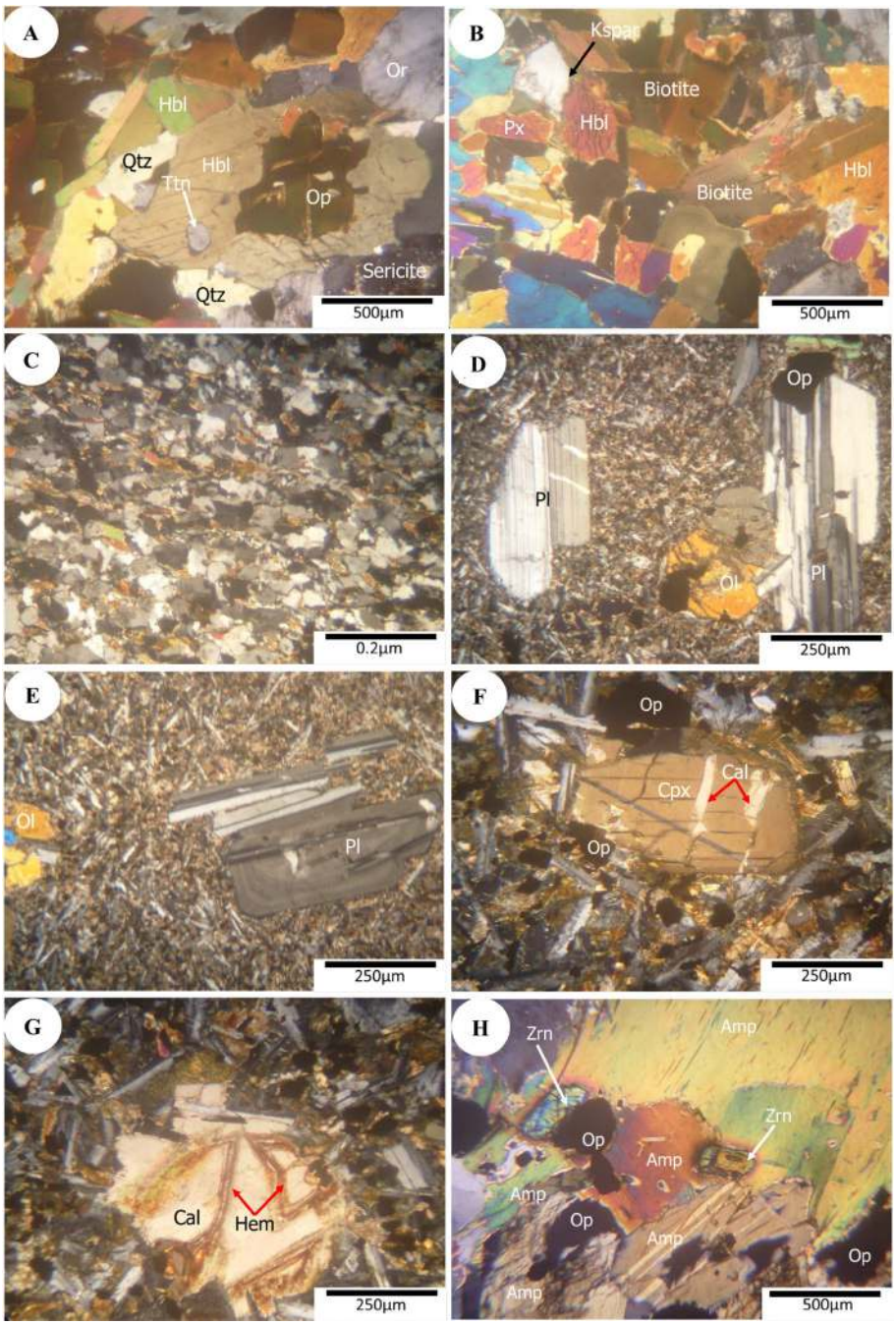

Fig. 2 Photomicrographs of lithodemic units from Kitongo. Granodiorite (**A**, **B**): **A** Hornblende basal section showing diamond shape cleavage with titanite inclusion. **B** Fe–Mg mineral rich section in a porphyritic granodiorite with hornblende showing well developed twinning. **C** Mylonite texture marked by a foliated-like structure in fault zone. Microgabbro dykes with porphyritic texture (**D**, **E**). Lamprophyric dykes (**F**, **G**): **F** Clinopyroxene (Cpx) crystal displaying (010) cleavage planes with some transversal fracture showing a starting alteration to calcite. **G** Calcite (Cal) mineral displaying oscillatory zoning with respect of Ca and Fe (hematite) and a jigsaw-like aspect. Granitic facies of the Kitongo pluton (**H**–**P**): **H** Amphibole (Amp) granite with interlocked of amphibole mineral and inclusion of zircon crystals displaying radiohalos. **I** Granite displaying euhedral amphibole with interlocked feldspars. Some orthoclase crystals may develop perthite. **J** Anhedral coarse grained orthoclase developing sericite associated with titanite (Ttn) and amphibole minerals. **K** Monazite (Mnz) inclusion displaying radiohalos in amphibole phenocrystal. **L** Zircon (Zrn) inclusion displaying radiohalos in amphibole phenocryst. **M** Myrmekitic exsolutions around orthoclase. **N** Perthitic orthoclase phenocrysts. **O** Granite with interlocked amphiboles displaying disseminated radiohalos caused by the inclusion of minute undertermined radioactive minerals within the host amphibole minerals. **P** Bent spindle plagioclase highlighting a plastic deformation around orthoclase of with cloudy aspect and quartz displaying

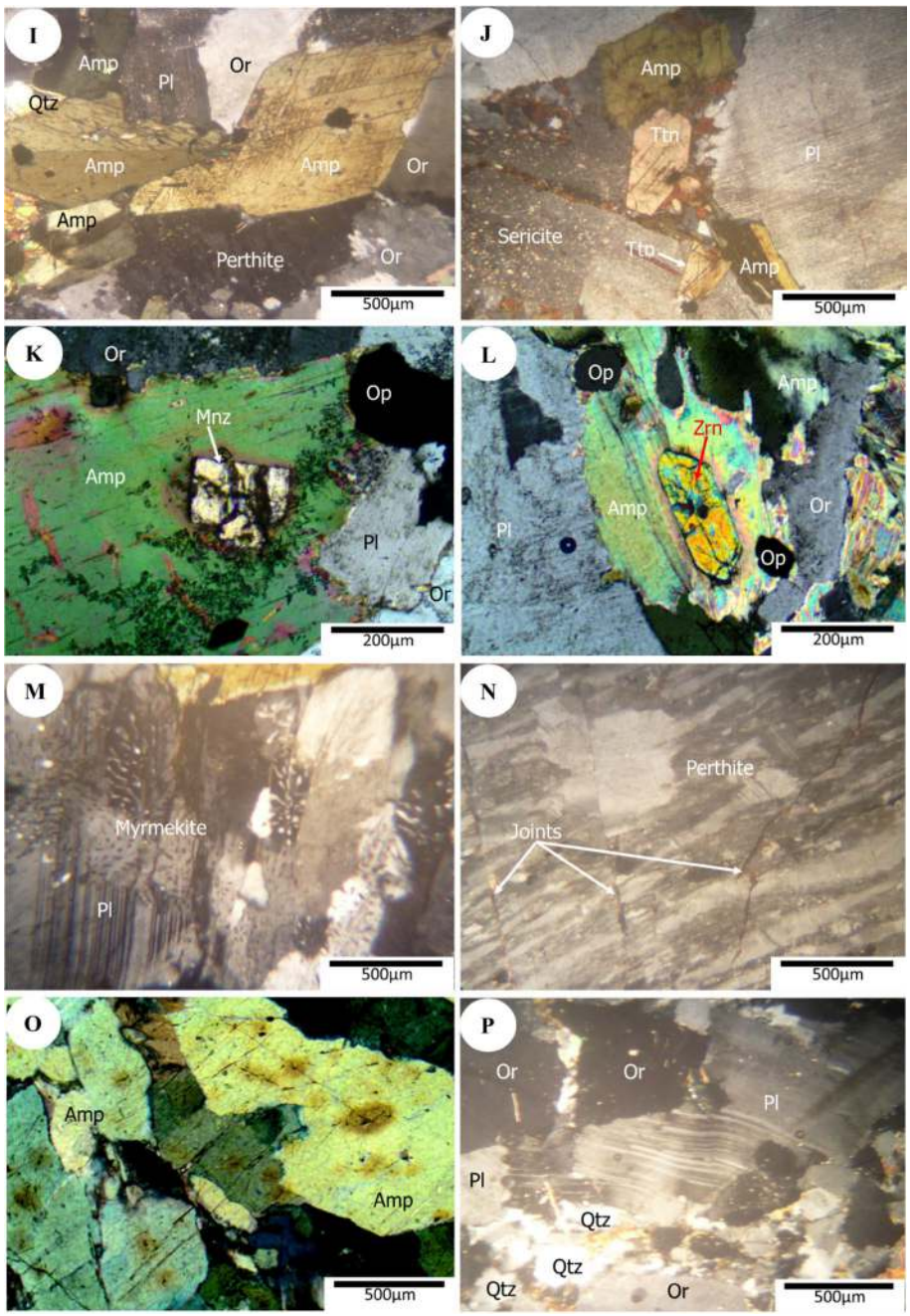

Fig. 2 (continued)

as a result of hydrothermal alteration of amphibole. Calcite occurs widespread in the breccias either as individual crystal or may form clusters (Fig. 3j), it may also fill late micro-fractures (Fig. 3a, d) and may probably derive from Ca liberated during the albitization of magmatic plagioclase or the retrogression of Ca-rich amphibole. In the Fig. 3k, uranium minerals form disseminated grains and show close symbiosis with Ab2; in certain areas uranium minerals may form cluster with ovoid shapes. Under the polarized reflected light, uranium mineral exhibit zoning characterized by different brightness from core outward, suggesting chemical differences in these zones (Fig. 3l). Accessory minerals in the brecciated albitites are monazite, epidote, titanite, apatite and zircon crystals forming clusters in opaque phases and amphibole crystals (Table 1; Figs. 3f and 5). Pervasive alteration of the breccias is marked by retrogression of plagioclase into sericite as well as hematite staining of the rock matrix (Fig. 3a, i).

U-ore phases in the breccias from the KSZ are spherical with a mineral nucleus (Figs. 4 and 5b, c), massive aggregates (enclosed in albite and riebeckite; Fig. 5d, g), or veinlets (Fig. 5e). BSE observations show that micro-fractures in these breccias provided pathways for the circulation of hydrothermal and possibly surface-derived fluids which significantly affected the structure of the primary U-minerals (Fig. 5b, d, h). Some of these U-minerals show areas of various brightness (Fig. 5c), reflecting the heterogeneous composition of U-mineral phases that were found composed of variable amount of Na, P, Ca, Th, Fe, and U contents (Fig. 4). Moreover, radiation damage aureoles develop around idiomorphic uraninite crystals due to the effect of alpha radiations in enclosing magnetite crystals resulting into newly formed mineral phases (Fig. 5b, c).

Chemistry of U-ore phases

A combined analysis of the results from SEM maps and WDS confirmed the chemical heterogeneity of U-bearing minerals pointing to variation in types, abundance and occurrence modes of the U-phases in the studied ore bodies (Table 2; Figs. 5, 6, 7 and 8). Typical BSE images of the studied U-ores are displayed in Fig. 5a–h. The main element concentrations (U, Si, Zr, Fe and Ca) in the identified uranium ore phases from the studied samples e.g. uraninite, coffinite, U–Zr–Si, U–Fe–Si, and U–Ti alloys show significant variations (Table 2, Fig. 6). The aforementioned U-ore phases are here after separately described.

Uraninite

Uraninite forms disseminated euhedral to anhedral grains (Figs. 4 and 5a) and aggregates mainly in albite and riebeckite. Detailed observations revealed that some uraninite minerals develop typical radial fractures in enclosing minerals (Figs. 5b, d and h) which provided pathways for the circulation of late hydrothermal and surface-derived fluids. The percolation of these younger silica-rich solutions resulted in variable degree of coffinitisation of uraninite along the Kitongo shear zone. Zircon crystals can be found included in some other uraninite minerals (Fig. 5b). Figure 5c shows euhedral zoned uraninite with rounded destruction rim. This mineral exhibits areas of different intensity of gray color as a result of the alteration of uraninite or newly formed minerals as a consequence of percolating solutions. Table 2 shows that the chemical composition of uraninite minerals from the Kitongo shear zone varies as follows: UO_2 (65.90–66.59 wt.%), SiO_2 (0.84–1.14 wt.%), FeO (3.10–3.33 wt.%), CaO (2.78–2.85 wt.%), TiO_2 (1.13–1.24 wt.%) and Ce_2O_3 (1.07–1.08 wt.%) contents being higher than those of ThO_2 ($\leq$0.03 wt.%) and Al_2O_3 (0.02–0.04 wt.%). The significantly high CaO contents (2.78–2.85 wt.%) in these uraninites indicate that the mineralizing hydrothermal fluid was Ca-enriched. Later on, the primary uraninite was altered and the alteration process which is depicted by a loss of U concomitantly with an increase in Si-content occurred during an alteration process referred to as coffinitisation (Fig. 7a). Coffinitisation may have been a progressive phenomenon with the development of the coffinized-uraninite phase that is mainly characterized by intermediate values of UO_2 (52.41–73.20 wt.%), SiO_2 (2.90–6.92 wt.%), CaO (2.86–3.66 wt%) and FeO (2.86–22.15 wt.%). In addition, the TiO_2 content also increase and may reach up to 2.02 wt% (Table 2).

Fig. 3 Photomicrographs of hydrothermal alteration (**A**–**J**) and uranium ore (**K**, **L**) at Kitongo. **A** Brecciated hydrothermal U-ore body with calcite uranium (Cal-U) veins on outcrop. **B**–**D** thin sections highlighting breccia features: **D** two stages Na-alterations evidenced by two distinct albite generations. **E**–**J** mineral assemblage showing: **E** incipient transformation of orthoclase to albite. **F** amphibole (Amp) associated with albite (Ab2) and hydrothermal zircon (Zrn) clustering within the rock matrix. **G**, **H** Aegirine (Aeg) and riebeckite (Rbk) resulting from the alteration of amphibole with the liberation of magnetite (Mag). **I** Reddening of the brecciated albitite by hematite. **J** Cluster of calcite (Cal) around other hydrothermal minerals such as albite (Ab2), aegirine (Aeg). **K** Typical disseminated uranium ore showing globular uranium oxides within the brecciated albitite. **L** Reflected light image exhibiting the zoning structure of the globular uranium oxides characterized by different brightness from core outward ▶

Coffinite

Coffinite appears predominantly as pseudomorphs after uraninite. It also forms crystal intergrowths with uraninite or irregular disseminations within uraninite crystals. The coffinite-rich portions in these crystals are typically less bright in backscattered electron image than the core occupied by uraninite or U–Zr rich phases (Fig. 5c); this is due to the presence of Si with a lower atomic mass as compared to U. In addition, some of the U-ore minerals probably coffinized-uraninite, can form small-sized inclusions in albite crystals. Coffinite in association with secondary calcite forms micro-veinlets (generally less than 1 mm thick) cutting across the mineralized samples (Fig. 5f). Other micro-veinlets occur as short en-echelon veins exhibiting dextral or sinistral shearing movements (Fig. 5h). Such micro-veinlets mostly contain coffinite (Fig. 5e, f). The concentration of U and Si in coffinite from the studied samples were highly variable, ranging from 31.13 to 72.39 wt% and from 11.18 to 19.64 wt% respectively. It is worth noting that both U and Si depict a negative correlation in these U-bearing phases (Fig. 7a), thus pointing to an incompatibility between these two elements. Other elements also showed significant variations: CaO from 1.17 to 8.95 wt% and FeO from 0.52 to 37.13

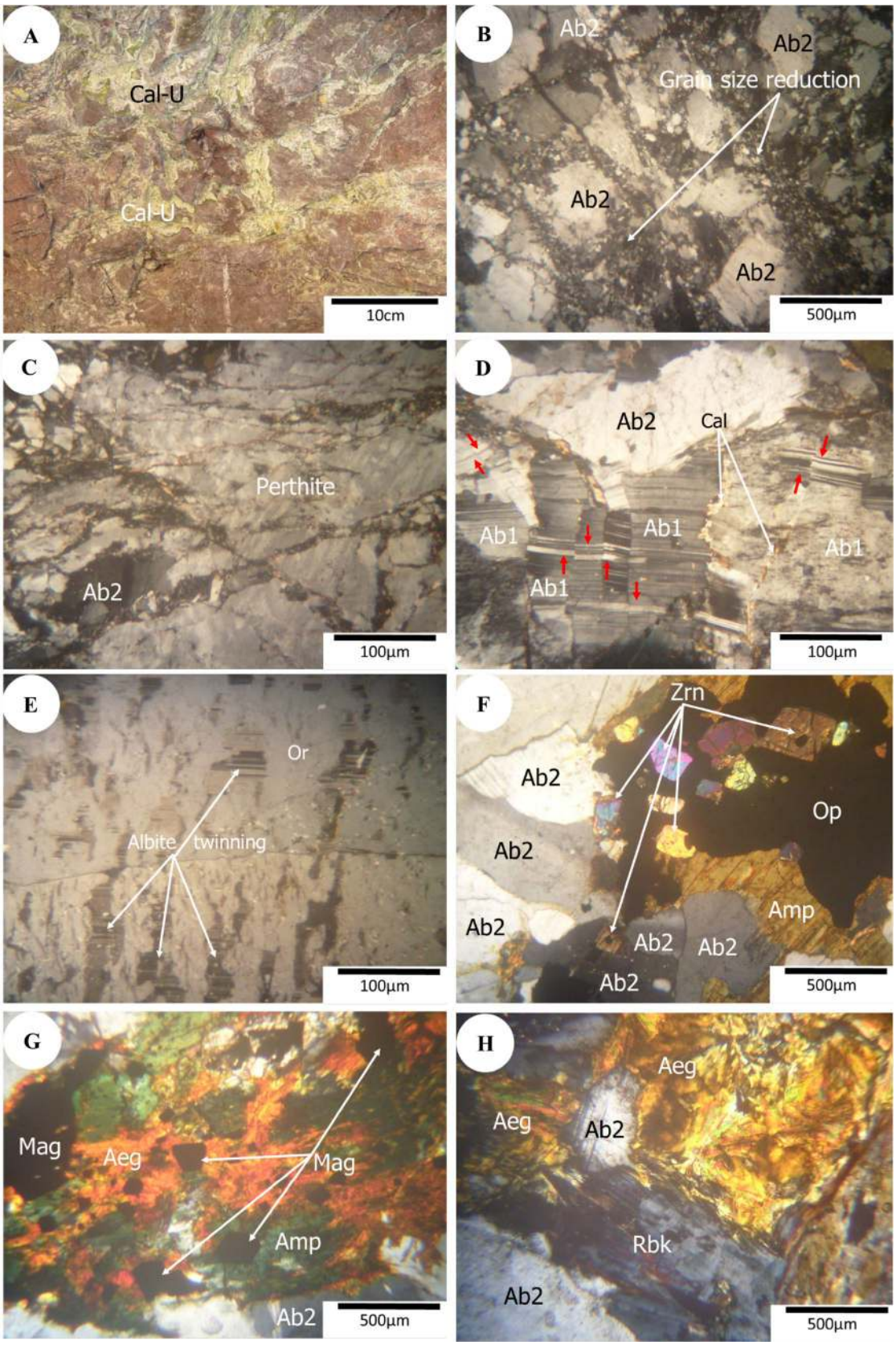
A
Cal-U
Cal-U
10cm
B
Ab2
Ab2
Grain size reduction
Ab2
Ab2
500µm
C
Perthite
Ab2
100µm
D
Ab2
Cal
Ab1
Ab1
Ab1
Ab1
100µm
E
Or
Albite twinning
100µm
F
Zrn
Ab2
Op
Ab2
Amp
Ab2
Ab2
Ab2
Ab2
500µm
G
Mag
Aeg
Mag
Amp
Ab2
500µm
H
Aeg
Aeg
Ab2
Rbk
Ab2
500µm

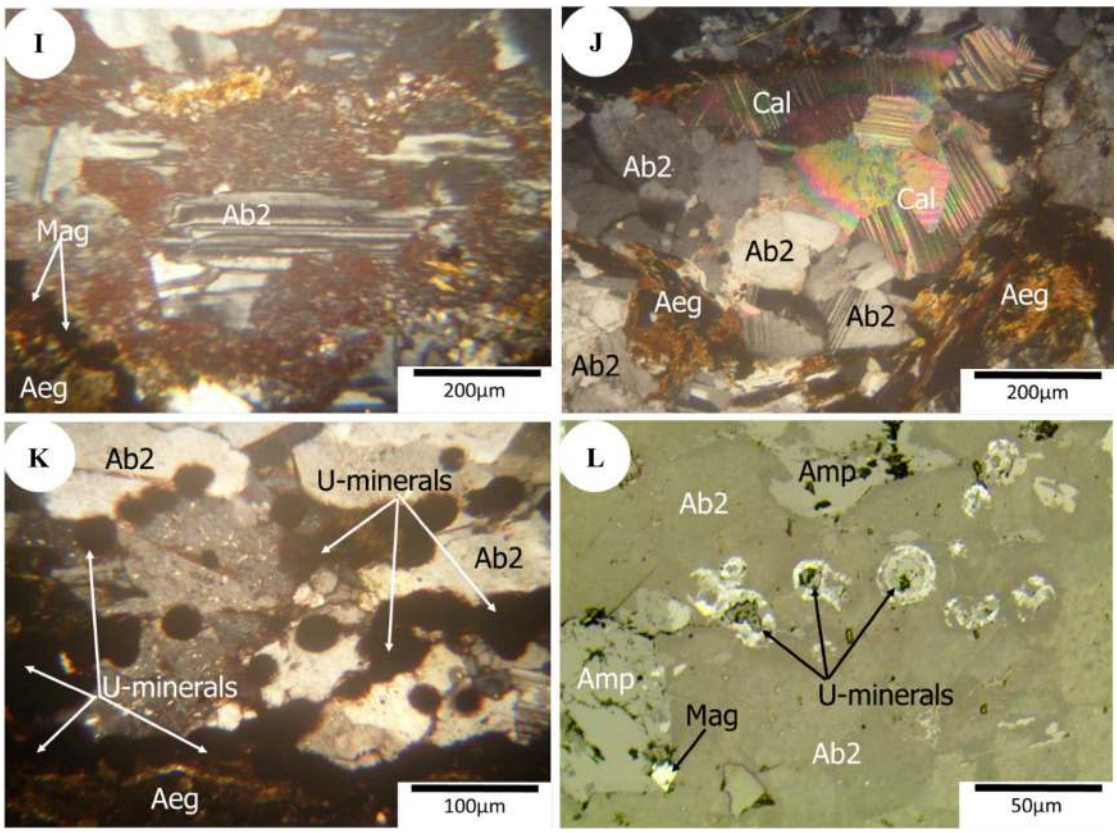

Fig. 3 (continued)

wt% (Table 2). Overall, the analytical data from the coffinite phase underline the heterogeneous chemistry of this phase.

U–Zr–Si phases

U–Zr–Si phases occur randomly distributed close to uraninite and coffinite-rich zones. Uranium content in these phases ranges from 25.08 to 51.36 wt%. The compositional range in this phase is consistent with a solid solution between the hydrate equivalent of $USiO_4$ and $ZrSiO_4$. Two groups of U–Zr–Si phases are distinguished: group 1 in which Zr contents vary from 3.41 to 11.74wt%; and group 2 with Zr contents ranging from 13.35 to 31.88 wt% (Table 2). The Ce_2O_3, ThO_2, P_2O_5 and CaO contents in group 1 are relatively higher than in group 2 (Table 2; Fig. 7b–e). The U–Zr–Si phases are generally Ti-depleted and Th–Ce enriched as compared to some other U-ore phases. In addition, the aforementioned phases appeared to be also heterogeneous.

U–Fe–Si phases

U–Fe–Si phases occur as a mix-product of materials from altered coffinite and magnetite mineral. They form anhedral mineral phases irregularly distributed in riebeckite minerals, and at the rim of uraninite and coffinite minerals (Fig. 5b, d) except in coffinite associated with secondary calcite in micro-veinlets. The WDS analysis show that the U–Fe–Si phases have the lowest U concentrations (5.73–15.51 wt% UO_2) as compared to the other U-ore phases (Table 2). Conversely, these phases show significant amount of oxides e.g. MgO (up to 3.57 wt%), Al_2O_3 (up to 6.30 wt%) and Na_2O (up to 5.21 wt%). This phase shows the highest Si content. Fe content in all the U-ore phases depicts a general negative correlation with respect to U (Fig. 7g) and thus suggesting an overall incompatibility between Fe and U in the U-ore phases in the brecciated albitites U-ores from Kitongo.

U–Ti phases

Only a small part of titanium mineral forms U–Ti phases and occurred as small anhedral phases enclosed in riebeckite crystals. The presence of the U–Ti phases in the studied samples was revealed by WDS analysis (Table 2). These U-phases present up to 21.10 wt% UO_2, and up to 16.01 wt% TiO_2. Ca showed considerable amount in these phases. In addition, the aforementioned phases content the highest P concentration relative to the other U-phases (Table 2). The P_2O_5 in the U-Ti phases depicts a negative correlation with

Table 1 Mineral paragenesis along the Kitongo shear zone established on the basis of petrographic study

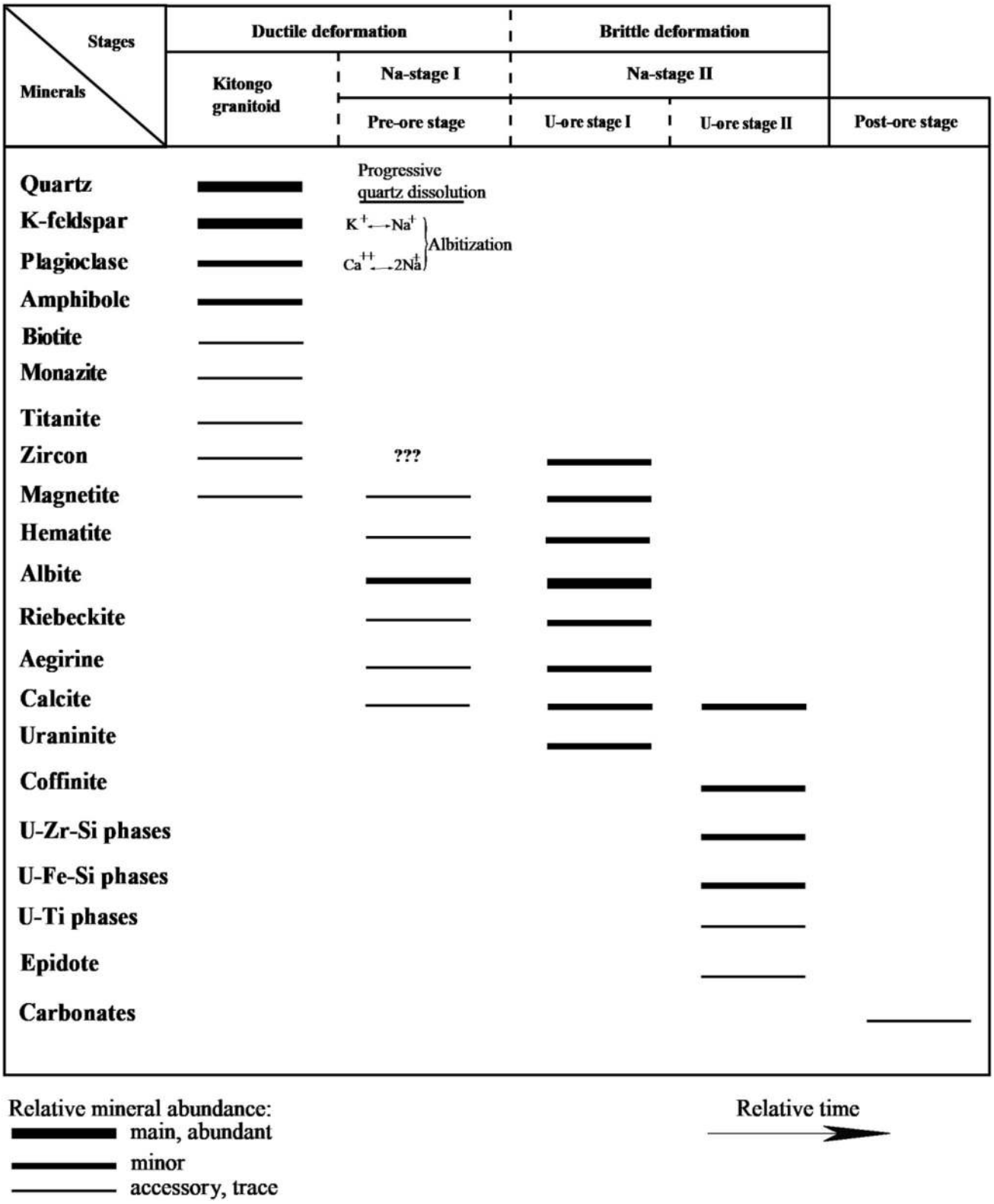

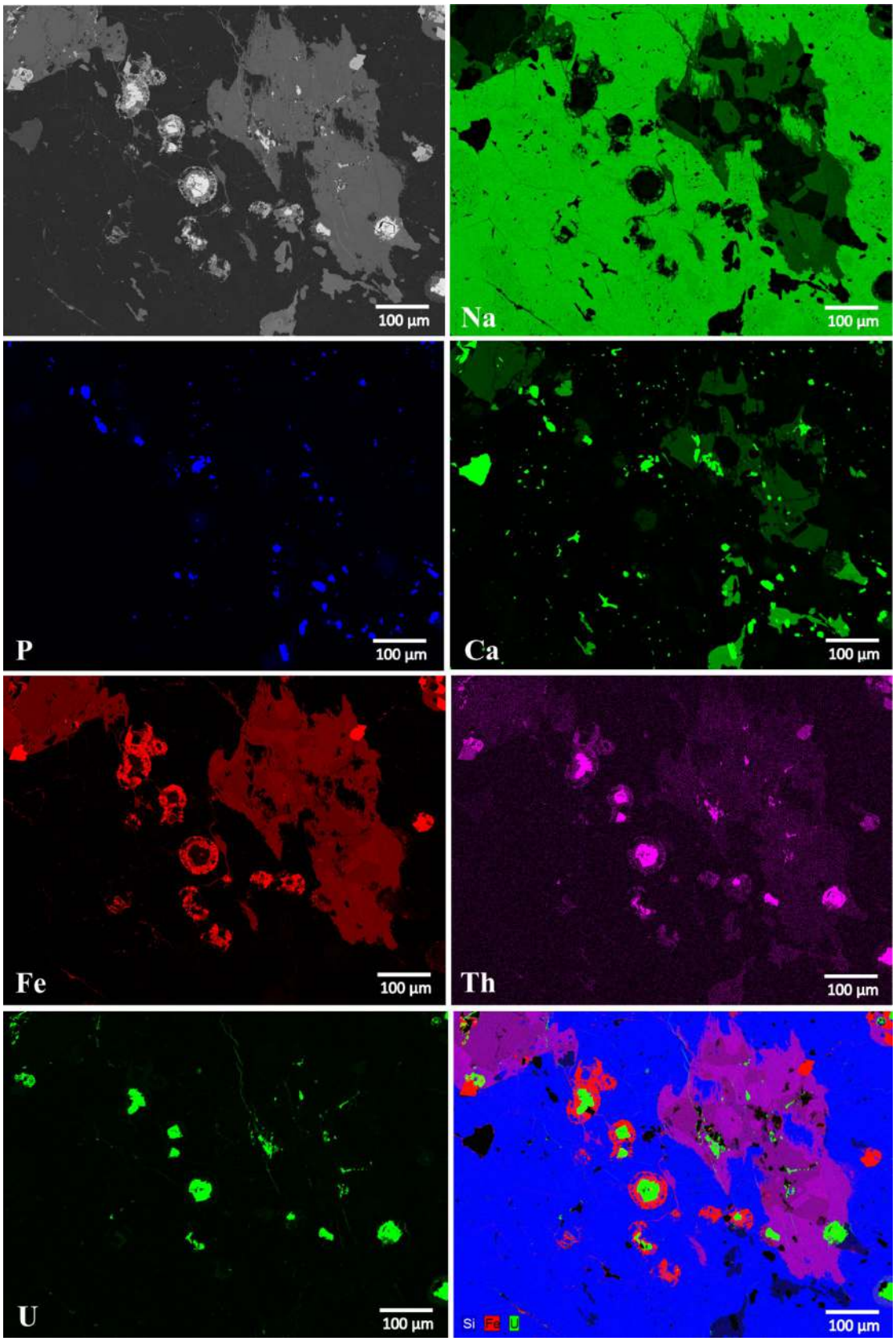

Fig. 4 Back-scattered electron (BSE) images and corresponding phase-patched mineral maps showing typical minerals and textures present in samples for Na, P, Ca, Fe, Th, U and a combination of Si–Fe–U

U together with the P_2O_5 content of some U–Zr–Si phases, coffinised-U, coffinite and uraninite (Fig. 7b).

Discussion

Tectonic setting and mineralogy of the initial granite

The Kitongo granite was generated under collisional tectonic context of the Pan-African orogeny which was still active after 580 Ma (Ngako et al. 2008). The last episode of that orogeny is manifested by ductile to brittle deformation that generated shear zones of various orientation within the CAFB. At Kitongo, the aforementioned fault system controlled the hydrothermally related U- mineralization that occurred at fault intersections of the ENE–WSW-trending faults and the overprinting Riedel shear types (Kouske et al. 2012). The petrographic study of the Kitongo granite has revealed that the texture of this rock varies from porphyritic to equigranular granite and the magmatic paragenesis of this granite is composed of K-feldspar, plagioclase, quartz, amphibole, zircon, titanite, monazite and biotite. Such a mineralogical composition suggests an I-type granite (Chappell and White 1992). In addition, the presence of subhedral to euhedral phenocrysts of minerals such as amphibole, titanite and zircon (Fig. 3c, d and f respectively) with some of them being observed filling interstices (i.e. quartz) suggest that the cooling of the magma and therefore the crystallization of these minerals from the magma was gradual (Bouchez et al. 1992).

Ore stages

Na-metasomatism related uranium mineralization during a two-stage albitization was described in the Kitongo U-deposit (Kouske et al. 2012). The first albitization stage (pre-ore stage) is marked by the development of myrmekite and perthite microtextures in this granite (Fig. 2m, n). Myrmekite develops under a reaction consuming residual melts (Phillips 1980a) but may also form at lower temperature (Phillips 1980b). Perthite occurs as the result of the dissolution–precipitation processes from fluids at temperatures ranging from 550 to 450 °C (Parsons and Lee 2009; Norberg et al. 2013). As such, the pre-ore stage may have globally occurred at high temperature. During this ore stage, albite (Ab1), magnetite, hematite, riebeckite, aegirine and calcite also formed (Table 1). Some albite (Ab1) minerals were crosscut by numerous micro-faults of dextral to sinistral kinematics highlighting marks of brecciation (Fig. 3d). Brecciation phenomenon over the Kitongo U-deposit occurred as the result of wrench faults reactivation through dilation jogs (Ngako et al. 2008). The resulting tectonic breccias grade from crackled breccias (Fig. 3c, d) to cataclastic texture (Fig. 3b). This observation fits well the aforementioned hypothesis of a phased brittle deformation along to KSZ. These tectonic breccias favored the circulation of the late Na-rich fluids and thus provoking the second albitization (U-ore stage I) event that overprinted the first one mostly at fault intersections. During that albitization event, quartz dissolution continued, and Fe–Mg minerals such as amphibole continued to be destabilized into aegirine, riebeckite, calcite (Fig. 3h–j) and apatite (Fig. 5b, e, f) with an increased intensity as compared to the first albitization event. Albite (Ab2) occurred either as pseudomorphic replacement of orthoclase (Fig. 3e) or newly formed albite crystallizing in quartz dissolution vugs (Fig. 3d). Generally, the pseudomorphic replacement albite contains no carbonate. Pores filling albite margins are irregular (Fig. 3d, f, h and j). Twinning is generally not well developed in the Ab2. In addition to these mineral transformations, other minerals formed including: magnetite, hydrothermal zircons, titanite and U-oxides. This paragenesis is comparable to those from other Na-metasomatic-related U deposits (Grechishnikov et al. 1977; Polito et al. 2009; Cuney et al. 2012; Mosoh Bambi et al. 2012; Embui et al. 2019; Vanderhaeghe et al. 2020; Bute et al. 2020). The studied brecciated albitites are pinkish to reddish in color, suggesting that the brecciated ore bodies along the KSZ were impregnated by hematite resulted from the late oxidation of magnetite; generally, hematite forms tin rims around magnetite crystals. Moreover, this impregnation processes of breccias along the shear zone may have been synchronous with the U-ore stage II during which U-silicates, calcite and epidote formed (Figs. 3 and 5). A similar scenario was observed in the Australian deposits (Wilde et al. 1989), in the shear zone hosted late Variscan and post-Variscan hydrothermal U-mineralization (Kribek et al. 2009) and in the Bor granite (René 2017). It can therefore be suggested that the Kitongo U-deposit underwent oxidations with possible mixtures with reducing fluids during fluid-circulation events. The post ore stage is mainly characterized by the formation of carbonate (Table 1). Overall, four main stages of U-ore development were distinguished at Kitongo: (a) the pre-ore, (b) the primary ore stage, (c) secondary ore stage and (d) the post ore stage (Table 1).

Regional distribution of U- deposits and source of the mineralizing fluids

Previous studies have identified significant U deposits within the Eastern Nigeria Terrane (ENT) as well as in the contiguous CAFB. In the ENT, two uranium mineralizing episods were distinguished in the Mika deposit located within the Adamawa Massif. These U-mineralizations are structurally controlled as follows: (a) the primary U-mineralization mainly made up of pitchblende, uraninite and brannerite is

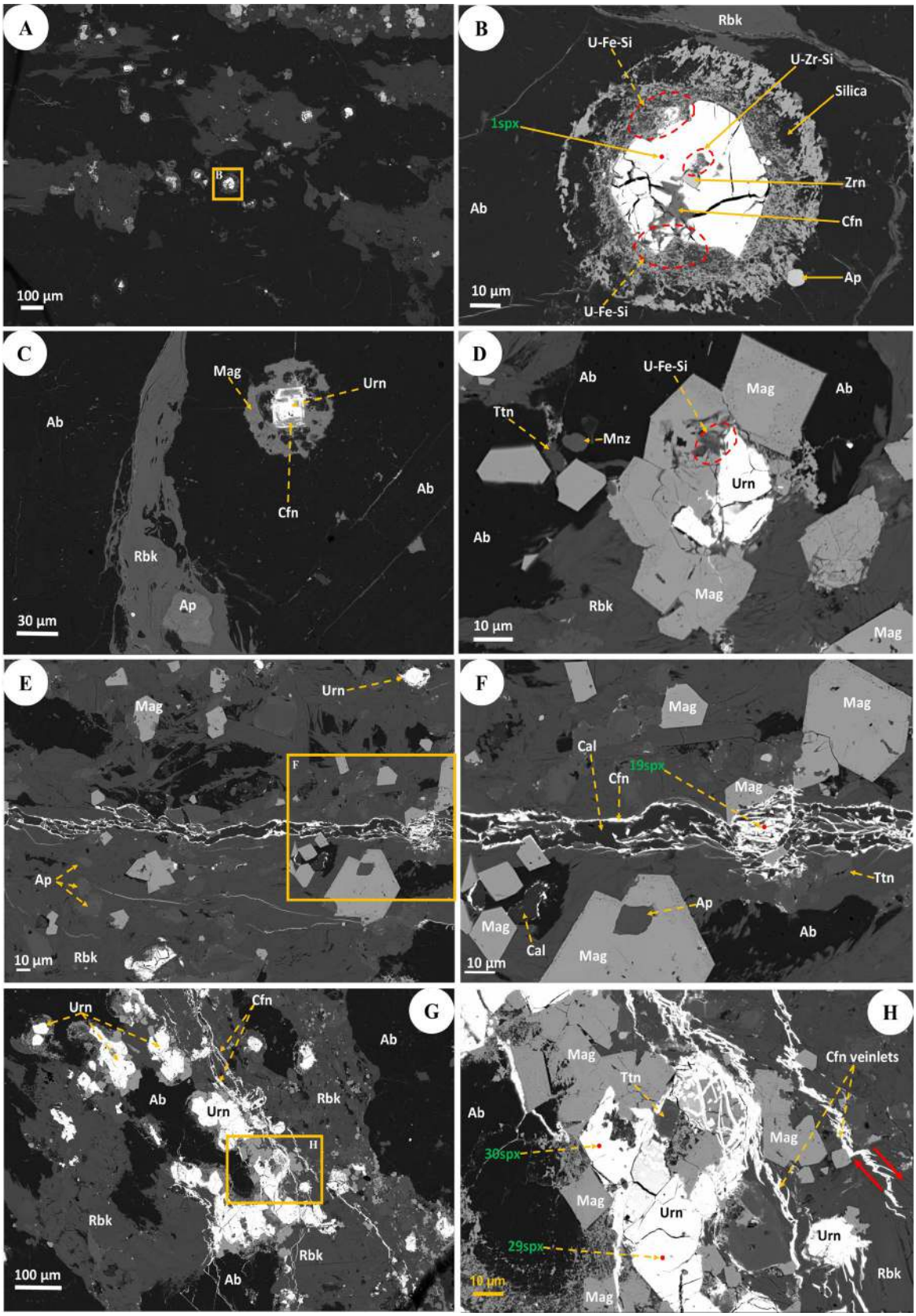
A
B
100 µm
B
Rbk
U-Fe-Si
U-Zr-Si
Silica
1spx
Zrn
Ab
Cfn
Ap
10 µm
U-Fe-Si
C
Mag
Urn
Ab
Ab
Cfn
Rbk
Ap
30 µm
D
Ab
U-Fe-Si
Mag
Ab
Ttn
Mnz
Urn
Ab
Rbk
Mag
10 µm
Mag
E
Urn
Mag
F
Ap
10 µm
Rbk
F
Mag
Mag
Cal
19spx
Cfn
Mag
Ttn
Ap
Mag
Ab
Cal
Mag
10 µm
G
Urn
Cfn
Ab
Ab
Rbk
Urn
H
Rbk
Rbk
100 µm
Ab
H
Mag
Cfn veinlets
Ttn
Ab
Mag
30spx
Mag
Urn
Urn
29spx
Rbk
10 µm
Mag

◂**Fig. 5** Backscatter electron images of uranium phases in the brecciated albitites U-ores from the Kitongo deposit. **A** Disseminated and anhedral uranium grains; **B** magnified view of the box from the image **A**, showing a typical radiation damage aureole around idiomorphic uraninite crystals with the development of newly formed U–Fe–Si phase, uraninite with high reflective area is cross cut by radial fractures where coffinite (Cfn) develops with inclusion of euhedral zircon, alteration of zircon (Zrn) together with silica and uraninite leading to the U–Zr–Si phases. **C** subhedral uraninite showing progressive transformation (appearance of a lower backscatter image contrast) to coffinite and surrounded by a radiation damage aureol of magnetite within a matrix comprised of albite (Ab), riebeckite (Rbk) apatite (Ap). **D** Homogeneous euhedral magnetite (Mag) with uraninite (Urn) at its core developing an incipient metamictisation at its contact with magnetite; titanite (Ttn) and monazite (Mnz) are also present. **E** A scanning electron micrograph image and its magnified view (F) of a 15-µm wide of coffinite veinlet (19spx; Fig. 8a) that cuts the Mag–Rbk–Ab–Ttn matrix. Coffinite (Cfn) is alongside associated with calcite (Cal). Note the partial destruction of magnetite grain by the veins and its contents. **G** A scanning electron micrograph image and its magnified view (**H**) showing uraninite (Urn) that cluster in the close proximity with magnetite (Mag) generating metamictisation. Coffinite also appear as stockwork or microveinlets developed thanks to tension gashes in en-echelon suggesting that at least an episode of uranium circulation during syn to post brittle deformation

related to albitization along the early N-S trending normal faults; (b) while the N130E transpression zones concentrate the secondary uranium autunite ores resulting from a remobilization of uranium from primary ores (Suh and Dada 1998). In the Kanawa prospect, U-mineralization is controlled by a norrow N-S shear zones. According to Bute et al. (2020), this U-mineralization is associated with K, Na and Ca hydrothermal alterations. In the CAFB, the Kitongo U deposit shares some similarities with the Zabili U deposit in Chad Republic (Vanderhaeghe et al. 2020). Both deposits underwent a two stage albitization; the second albitization stage characterized by Na–Ca-metasomatism associated to brittle faults cross-cutting the NE to ENE-trending ductile shear zones is synchronous U-mineralization. In the SW of Cameroon, the Ekomédion U–Mo prospect occurs in the Ngondo Complex (Mosoh Bambi et al. 2012). Rocks in this complex are mainly syn-to post-tectonic high-K calc-alkaline Pan-African granites. The U–Mo is locally hosted by a highly fractured granite along the NE-SW regional faults (Mosoh Bambi et al. 2013; Embui et al. 2019). As a whole, the geological locations of these individual U-deposits and their structural attributes suggest that they may have had the same structural controlling fault systems: the Pan-African–Brasiliano shear zones that may have favoured the implacement of the aforementioned U-deposits as well as U-deposits in the Borborema Province, NE Brazil including the Espinharas and Itataia deposits (Verissimo et al. 2016; Cavalcanti et al. 2018; Fig. 9).

Regarding the source of the Na and U mineralizing fluids in the Kitongo U-deposit, direct evidences are still lacking. However, the host rocks of this deposit is quite comparable to those of the Zabili U-deposit (Neoproterozoic meta-volcanic-sedimentary rocks) within the CAFB. Vanderhaeghe et al. (2020) suggested that host rocks of the Zabili U-deposit in Chad Republic do not contain neither a significant proportion of U-bearing minerals such as zircon, monazite or uraninite, nor salt-rich evaporitic units or marine sediments. For those authors, the most likely source for Na and U are the Zabili granite. Chen et al. (2012) suggested that halogens and volatiles play a key role in U enrichment and may be found in minerals such as apatite, amphibole and titanite. Although the hologens and volatiles were not studied, the aforementioned minerals have been observed in the Kitongo brecciated U-ores (Figs. 2, 3 and 5). Therefore, it can be inferred that those minerals may have yielded halogens which contributed, at least for a part, to U-enrichment at Kitongo. Another possible source of Na-metasomatic fluids and U mineralization may likely derive from convective fluids associated with the post collisional magmatic events manifested by Paleozoic–Mesozoic volcanism or the syenites of the Tertiary ring complex in the Poli area (Oesterlen and Vetter 1986); and the numerous mafic dykes cutting through granitoids (Kouske et al. 2012) and basement rocks (Kouske 2013).

Chemical composition of U-phases

The textural features and microchemical composition of the uranium-bearing phases in the brecciated albitites from the Kitongo U-deposit have enabled to identify uraninite, the unique primary U-mineral in the studied samples. The chemical composition and physical properties of the fluids related to the Kitongo granite and structures may have governed the alteration of primary U-mineral (Ram et al. 2013), producing secondary U-bearing phases (Finch and Kotzer and Kyser 1993; Murakami 1999) dominated by coffinite, U–Zr–Si, U-Fe-Si and U-Ti phases respectively. These phases were recognized in and around the core of primary phases yielding a micrometric scale of chemical heterogeneity of primary uraninite. Similar observations have been made in other deposits worldwide (Isobe et al. 1992; Janeczek and Ewing 1995; Kempe 2003).

Uraninite

The chemical composition of uraninite obtained from SEM-WDS was relatively variable (Table 2). The analytical totals ($n = 12$) ranged from 72.8 to 96.77 wt.% suggesting significant oxidation and/or hydration of the mineral (Alexandre and Kyser 2005; Zacharias et al. 2008). UO_2 content in the primary U-bearing phase ranged from 52.4 to 73.20 w%. The FeO contents were highly variable with values ranging from 2.86 to 22.15 wt.%. Thorium concentration in uraninite is low (less than 0.1 wt.%; Table 2). Low Th concentration

Table 2 Chemical composition of U-bearing phases in the brecciated U-ores from the Kitongo shear zone (northern region of Cameroon)

Locality	Kitongo																															
Paragenesis	Primary													Secondary																		
Mineral/phase	Uraninite			Coffinized-U										Coffinite								U–Zr–Si							U–Fe–Si			U–Ti
Form	Grains			Around or in uraninite «ghost»										Around uraninite grains or along fractures								Around grains or in ghost mineral							Around grains or in ghost mineral			Around grains or in «ghost» mineral
Sample	44	45	46	16	17	18	20	21	30	47	54	56		7	8	22	31	41	61	64	76	78	25	26	27	68	72	73	79	9	12	13	5
Na_2O	0.06	0.06	0.13	0.07	0.02	0.07	0.04	0.09	0.06	0.15	0.27	0.22		0.67	0.44	0.28	0.03	0.08	1.21	0.67	0.13	0.82	0.01	bdl	bdl	0.49	1.65	0.81	1.22	1.28	5.21	0.81	0.18
TiO_2	1.13	1.17	1.24	0.06	0.05	0.06	0.06	0.08	0.18	2.09	1.69	0.83		0.99	1.47	0.06	0.09	1.05	1.74	0.84	0.04	0.38	0.03	0.01	0.01	0.05	0.19	0.14	0.15	0.64	2.02	0.53	16.05
FeO	3.11	3.33	3.10	5.84	2.86	2.99	7.80	22.15	5.61	2.91	4.10	10.80		5.03	4.08	37.13	9.04	5.14	1.88	4.82	0.52	5.92	9.93	15.47	12.01	5.39	2.21	1.75	1.39	18.60	27.27	19.93	6.01
Al_2O_3	0.04	0.02	0.04	1.63	0.48	0.55	0.91	2.06	0.12	0.18	0.04	0.27		0.62	0.83	5.36	1.42	0.84	0.23	0.54	0.10	1.21	1.33	1.91	1.52	2.30	0.44	0.34	0.30	5.52	1.09	6.30	1.46
K_2O	bdl	bdl	0.03	0.04	bdl	bdl	bdl	0.13	bdl	0.32	0.12	0.16		0.03	0.14	1.15	bdl	0.75	2.37	1.27	2.49	3.80	bdl	0.09	0.03	0.57	0.32	0.56	1.66	1.00	0.26	1.04	0.29
MgO	0.04	0.05	0.06	0.23	0.05	0.06	0.06	0.12	0.11	0.07	0.05	0.08		0.52	0.51	0.17	1.18	0.33	0.06	0.15	0.03	1.14	0.18	0.27	0.20	0.66	0.19	0.24	0.16	3.57	3.38	2.53	0.56
ZrO_2	0.05	0.03	0.06	0.04	0.05	0.06	0.09	0.06	0.11	0.09	0.07	0.38		0.10	0.11	bdl	0.08	0.53	1.01	1.20	0.03	0.13	13.35	31.88	22.76	11.79	6.21	3.41	3.41	0.09	0.02	bdl	bdl
Ce_2O_3	1.07	1.07	1.08	0.93	0.87	0.63	0.81	0.64	1.45	0.51	0.95	0.68		1.33	1.29	0.05	0.72	bdl	0.82	3.80	0.06	0.56	0.71	0.33	0.47	2.04	3.16	2.27	2.47	0.31	bdl	0.07	0.80
SiO_2	0.85	0.84	1.14	6.53	4.54	6.28	5.64	6.92	6.00	2.90	3.28	3.57		15.98	15.77	14.26	17.40	15.06	12.48	11.18	14.75	19.64	12.84	21.84	17.59	21.48	16.31	11.59	15.42	31.62	44.56	35.09	13.61
CaO	2.78	2.85	2.83	2.67	2.99	3.17	3.14	2.62	3.45	3.16	3.66	3.20		5.47	5.31	2.87	2.30	8.95	1.37	2.49	2.45	1.17	2.84	1.99	2.71	1.56	1.79	24.50	1.78	2.43	1.23	8.73	12.55
ThO_2	0.03	bdl	bdl	0.08	0.06	0.13	0.28	0.26	0.14	0.01	bdl	0.00		bdl	0.05	bdl	0.07	0.01	0.62	1.27	bdl	0.24	0.11	0.05	0.10	2.27	1.36	1.36	1.30	bdl	0.02	bdl	0.01
P_2O_5	0.05	0.03	0.04	0.07	0.06	0.07	0.07	0.07	0.15	0.07	0.07	0.08		0.31	0.38	0.05	0.08	0.12	0.62	0.62	0.13	0.38	0.25	bdl	0.09	0.75	0.88	0.92	0.87	0.13	0.05	0.12	0.93
UO_2	65.90	66.59	66.30	67.50	71.79	71.08	73.20	61.33	70.26	61.97	60.63	52.41		54.65	56.53	31.13	46.55	55.34	60.49	38.27	72.39	51.76	51.36	25.08	40.58	36.60	44.72	32.25	50.14	15.51	5.73	13.10	21.10
SO_2	0.01	0.00	0.01	bdl	bdl	bdl	bdl	0.01	bdl	0.00	0.04	0.03		0.05	0.05	0.07	bdl	0.02	0.11	0.13	0.03	0.11	bdl	0.02	0.01	0.11	0.04	0.54	0.03	0.06	bdl	0.02	bdl
MnO	0.29	0.29	0.29	0.23	0.33	0.41	0.37	0.22	0.07	0.10	0.06	0.09		0.14	0.10	0.07	0.12	0.03	0.05	0.31	bdl	0.16	0.20	0.12	0.18	0.12	0.17	2.24	0.10	0.15	0.38	0.61	0.16
Total	75.32	76.16	76.29	85.90	84.07	85.49	92.44	96.77	87.41	74.53	75.01	72.81		85.87	87.05	92.63	78.93	88.19	85.08	67.54	93.14	87.40	93.11	98.51	98.21	86.18	79.65	82.91	80.39	80.89	91.21	88.85	73.65

This composition was obtained through SEM-WDS microanalysis

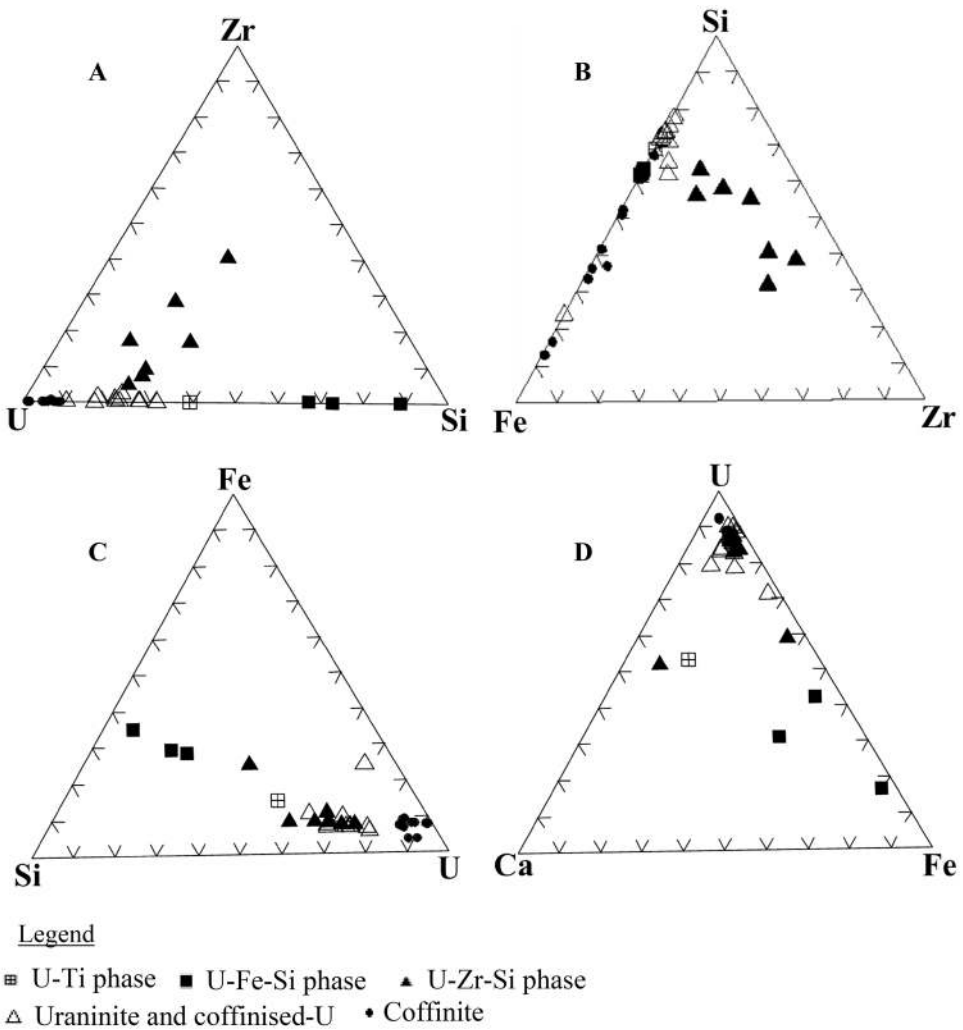

Fig. 6 Ternary diagrams illustrating range in composition of uranium phases in the brecciated U-ores type from the Kitongo U-deposit with respect to (**A**) U–Zr–Si, (**B**) Si–Zr–Fe, (**C**) Si–Fe–U and (**D**) U–Fe–Ca

have been found in uraninite from other uranium deposits related to Na-metasomatism (Cuney et al. 2012) suggesting a relative low temperature during the formation of these uraninite grains. Uraninite is known to be chemically reactive and readily exchanges elements or recrystallizes during post crystallization fluid-circulation events (Finch and Ewing 1992; Kotzer and Kyser 1993). For Alexandre and Kyser (2005), Ca is the main U replacing element in uraninite structure. Uraninite in the brecciated albitites from Kitongo showed a chemical age of 437 Ma (Maruejol 1989). WDS analysis revealed a variable CaO concentration which may reach up to 3.66 wt.% in these uraninite grains (Table 2) thus suggesting different stages of incorporation of this element during uraninite alteration.

Coffinite

Two varieties of coffinite have been observed in the brecciated albitites from the Kitongo U-deposit: (1) the replacement type coffinite and (2) the vein type coffinite. Textural features and microchemical composition of U-bearing phases in these brecciated albitites U-ore bodies show that the replacement type coffinite result from the progressive alteration of primary uraninite by younger silica-rich fluids of Si contents $> 10^{-2.7}$ mol/l (Brookins 1975), leading to variable degree of U-loss and an increase of Si, Fe and Ca in the structure of the coffinite (Table 2). The progressive conversion of uraninite to coffinite is manifested by the occurrence of an intermediate coffinitised U-phase (Table 2) and the rate of this conversion has resulted in the variegated textures of these U-phases (Fig. 5b, c). The coffinitisation of uraninite has been observed in other U-deposits (Goldhaber et al. 1987; Pointer al. 1989; Janeczek and Ewing 1992a, b; Savary and Pagel 1997; Bros et al. 2003) under reducing conditions and the gradual and repeated coffinitisation of uraninite were described from vein-type uranium deposits at the Massif Central in France (Leroy and Holliger 1984; Fojt et al. 2005 in René et al. 2019). Fluids circulation at the Kitongo U-deposit leading to the conversion of primary uraninite to coffinite may have at the same time deposited

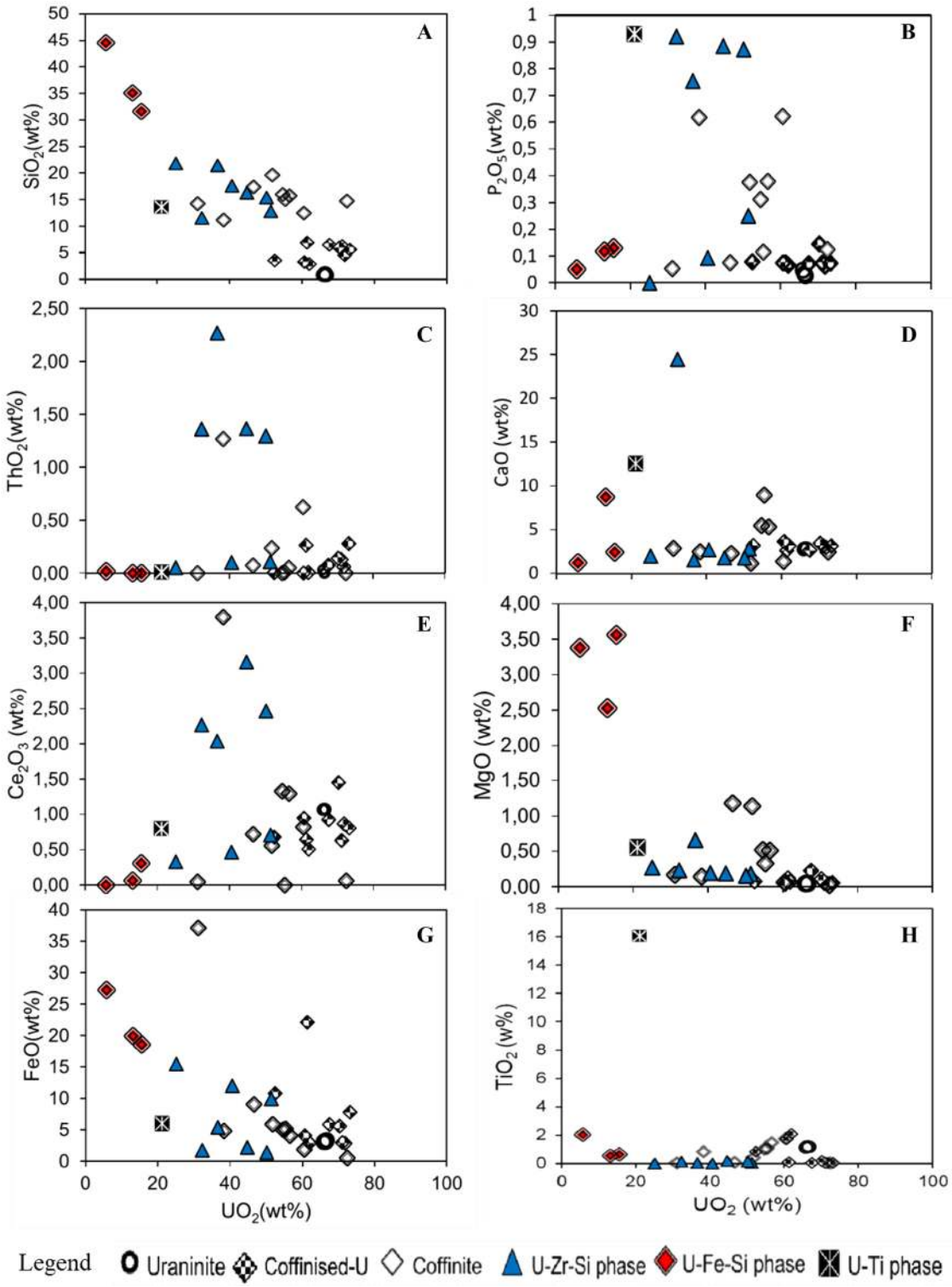

Fig. 7 U versus Si, P, Th, Ca, Ce, Mg, Fe and Ti contents (in weight percent) of different U-bearing phase from the Kitongo U-deposit. The name of mineral phases are quoted in the legend

coffinite along the fractures (veins type coffinite). Although the age of these two coffinite occurrence modes was not investigated, the vein type coffinite shows that at least an episode of uranium migration has occurred following the contact of silica-rich aqueous fluids with dissolved uranium in a reducing environment. This observation demonstrates

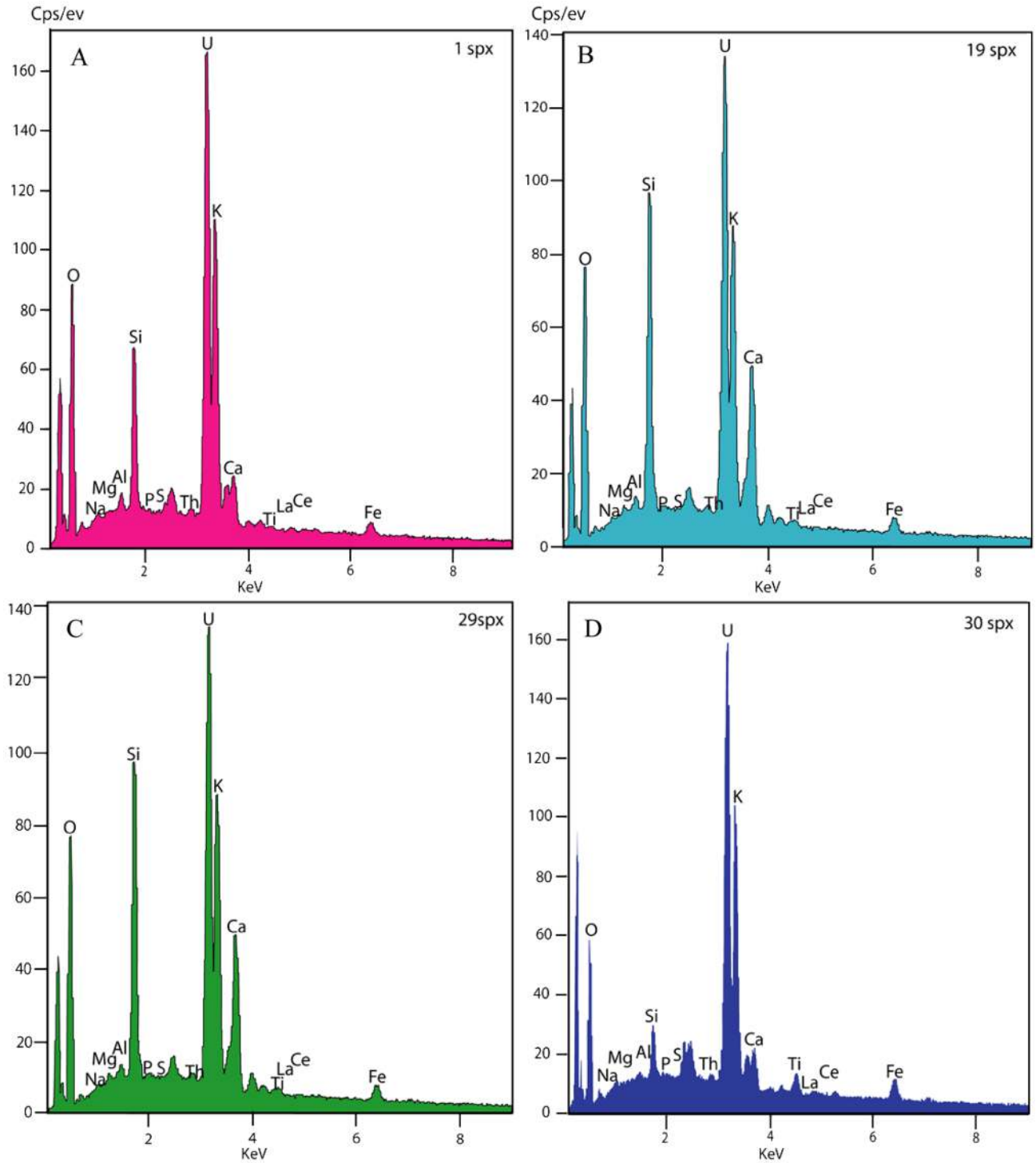

Fig. 8 SEM/WDS wavelength dispersive X-ray (WDS) spectrum for selected sample points on uranium minerals: (**A**), (**B**), (**C**) and (**D**) represent WDS spectra of points 1 spx, 19 spx; 29 spx and 30spx respectivily (Fig. 5)

a dip brittle phenomenon in the studied ore bodies (Polito et al. 2009). In addition, the close association of coffinite and calcite in vein type coffinite (Fig. 5e, f) suggests that dissolved U was transported as stable carbonate complexes at low-T (Hu et al. 2008). CaO contents in coffinite were found slightly higher than those in the uraninite (2.62–3.66 wt.% CaO) and varied from 1.17 to 8.95 wt.% CaO (Table 2). Accordingly, the aforementioned gradational integration of

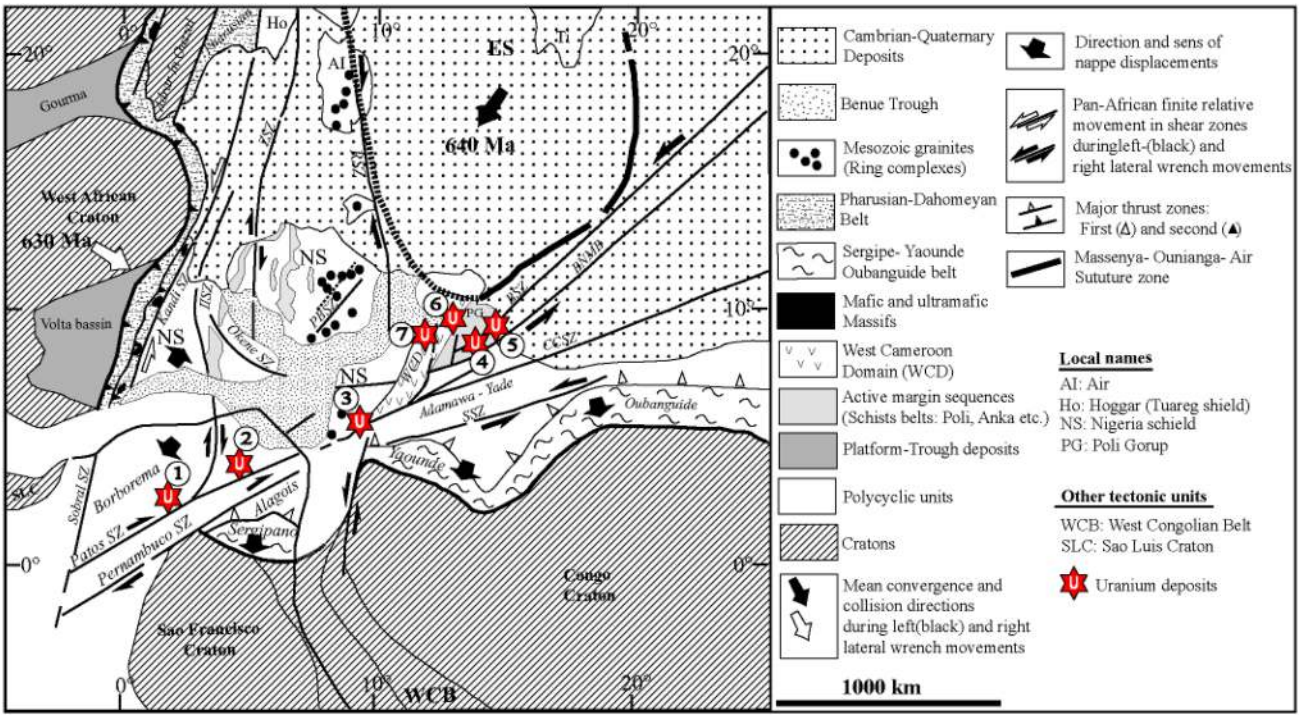

Fig. 9 Pan-African–Brasiliano shear zones in a pre-drift reconstruction. Finite sense of shear movement correlates with second tectonic event (black arrows) and third tectonic event (empty arrows) in northwestern Cameroon. Major and synthetic shear zones cross-cut earlier thrust and fold zones in all the Pan-African domains. Finite strain geometry displayed both by the left lateral wrench zones in northwestern Cameroon and the right lateral wrench zones of the Trans-Sahara–Nigeria–Brasilano domains outline a tectonic indent accommodating the shape of the eastern Saharan prong with locations of U- deposits: 1- Itataia; 2- Espinharas; 3- Ekomedion; 4- Kitongo; 5- Zabili: 6-Kanawa; 7-Mika (modified from Ngako et al. 2008)

Si, Fe and Ca during the conversion of uraninite to coffinite suggests that the hydrothermal alterations responsible for that converstion were episodic in nature.Thorium concentrations in the two occurring modes of coffinite (replacement and veins type coffinite) appeared very low ($\leq$ 1.27 wt.% ThO_2), probably resulting from the radioactive decay of the primary uraninite whose thorium contents were very low. Zirconium concentrations (up to 1.20 wt% ZrO_2) appear very low thus suggesting a weak incorporation of this element in the coffinite as compared to coffinite (up to 13.8 wt.% ZrO_2) from some shear-zones hosted hydrothermal uranium deposits in the Bohemian Massif, Central European Variscan belt (René and Dolnicek 2017). K_2O content (up to 3.08 wt.% K_2O) is interpreted as a contamination by minute K-bearing minerals (possibly illite).

U–Zr–Si phases

The U–Zr–Si phases occurred as U-silicates in the breccias from KSZ. The zirconium it contents is a high field strength elements (HFSE) which is generally considered immobile during hydrothermal processes (Bau 1996). However, strong complexation agents such as fluoride and phosphate anions may favour the mobility of this element in hydrothermal environments (Giére 1993; Chambefort et al. 2009; Migdisov 2009). The solubility of Zr also increases with the pH of fluids; and alkaline conditions are required for albitization. As such, zirconium enrichment appear to be a common feature in uranium deposits associated with Na-metasomatism (Rubin et al. 1993; Cinelu and Cuney 2006; Cuney and Kyser 2008) without F or P; and the highest Zr enrichment is observed in the Aricheng U-deposit in Guyana (Alexandre 2010). Kouske (2013) has shown that zirconium contents in the Kitongo U-mineralized samples may reach up to 1200 ppm; thus a portion of the U–Zr–Si phases identified during this study may result from that enrichment. The SEM-WDS analyses show that another portion of the U–Zr–Si phases occurs in the close vicinity of zircon inclusion in coffinised uraninite and thus may correspond to metamictized zircon due to radioactive decay of uranium from uraninite (Fig. 5b). Metamictization of zircon has been observed in other U-deposits worldwide; this phenomenon occurs when alpha radiations emitted from U and Th within the zircon lattice progressively destroy its original structure leaving amorphous materials. The chemical composition the U–Zr–Si phases is dominantly constituted by U, Zr and Si whose contents vary from 25.08 to 52.51 wt.%, 3.41 to 31.88 wt.% and 11.59 to 21.84 wt.% respectively and the majority of the analyses of the U–Zr–Si phases show higher

U contents than Zr (Table 2). Other elements such as Ce_2O_3 shows significant amounts (up to 3.16 wt.%) and may originate from hydrothermal alteration of original monazite (Broska et al. 2004). CaO contents in the U–Zr–Si phases is higher than those in uraninite and coffinite phases and vary largely (1.56–24.50 wt.% CaO). Phosphore contents reach up to 0.92 wt.% P_2O_5.

U–Fe–Si phases

The U–Fe–Si phases occur as a late feature with respect to sodium metasomatism. They appear irregularly distributed in the brecciated albitites U-ores as a result of interactions of altered primary uraninite and altered magnetite (martite?) and more rarely vein type coffinite and magnetite (Fig. 5b, d). These U-phases are dominantly composed of SiO_2 (31.62–44.56 wt.%); FeO (18.60–27.27 wt.%) and UO_2 (5.73–15.51 wt.%) respectively; wheareas, TiO_2 contents is up to 2.02 wt% (Table 2). Magnetite interactions with uranium bearing fluids have been explored by several authors (Dodge et al. 2002; Missana et al. 2003; Scott et al. 2005; Skomurski et al. 2011; Singer et al. 2012). Magnetite can remove U^{6+} from solution by its reduction to U^{4+} coupled to oxidation of Fe^{2+}, with precipitation of UO_2 on the magnetite surface. During this interaction in the system, other elements can be incorporated; this is the case for Ti which, together with U and Fe, yield the formation of U-ferropseudobrookite (Cuney et al. 2012). However the proportion of major components (U, Fe and Ti) of the U-ferropseudobrookite differ from those in U–Fe–Si phases studied here (Table 2).

U-Ti phases

The titanium necessary for the formation of U-Ti phase was probably released from the hydrothermal alteration of the Ti-rich accessory minerals (titanite). The chemical composition of U-Ti phases from the brecciated U-ore bodies (Table 2) is suggestive of the presence of brannerite which commonly occurs in uranium deposits associated to Na-metasomatism (Polito et al. 2009; Cuney et al. 2012; René et al. 2017). Smith (1984) has shown that U can be substituted by Ca, Th, Y, and REE, while Si, Al, and Fe can replace Ti either during the primary precipitation or during a later alteration episode especially for Ca, Si, Fe and Al. The calculated structural formula of U–Ti phases from the SEM-WDS analyses presents as follows: $U_{0.329}Ca^{2+}_{0.943}Ce_{0.017}Ti_{0.845}Al_{0.120}Si_{0.955}Fe^{2+}_{0.352}O_6$.

Conclusions

The brecciated albitite U-ores from the Kitongo shear-zone have revealed comparable features with other albitite-type uranium deposits worldwide. Their matrix consisted of strongly deformed granitoid under ductile and brittle regimes. Mineral association and the degree of alteration in the studied ores vary in type and intensity. The gangue minerals are mainly comprised of albite associated with variable amount of aegirine, riebeckite, magnetite, hematite and calcite together with a series of accessory minerals composed of epidote, apatite, and titanite. Albitization was also accompanied by newly formed zircons crystals in the brecciated U-ores. In these ores, uranium mineralization occurs as isolated euhedral to subhedral low-Th uraninite crystals, anhedral aggregates of uraninite crystals enclosed in albite and riebeckite crystals, and also as thin veinlets representing the latest U-mineralizing event. Vein type mineralization was mainly composed of coffinite which was associated to calcite. Disseminated and aggregates uraninite (up to 66.59 wt.% UO_2) represented the primary uranium phases. The secondary U-bearing phases deriving from the alteration of uraninite included coffinite (31.13–72.39 wt.% UO_2), U–Zr–Si (25.08–51.36 wt.% UO_2), U–Fe–Si (5.73–15.51 wt.% UO_2), and a U–Ti (brannerite?) type phase with up to 21 wt.% UO_2. Uraninite and coffinite are the most important U-phases in the studied ore samples. Uraninite and the other U-bearing phases showed always a very heterogeneous chemical composition. The oxidation of hematite and magnetite has produced the reddening of brecciated albitite that could have been responsible for the precipitation of primary uraninite. The conversion of uraninite into secondary U-bearing phases occurred during late hydrothermal and meteoric fluid circulations.

Acknowledgements We want to thank the Natural History Museum (NHM) in London for having facilitated the logistics and transportation of the studied samples to CERCAMS (Centre for Russian and Central EurAsian Mineral Studies) in Russia for thin sections manufacturation. We acknowledge the significant contribution of all the personnel of the laboratory IMPMC-UPMC, Paris, France where part of the analysis have been performed. This manuscript benefited from the review and comments from Jose Adilson Cavalcanti. We want to thank Professor Wolf-Christian Dullo and Madame Monika Dullo for the editorial handling of this work.

Author contributions The following is the CReDIT author statement. APK: conceptualisation-writing, editing, correcting and part of funding. MG: analyses and reviewing. JE: part of funding. NSK: reviewing. MST: reviewing TRG: reviewing and supervision. MC, reviewing SEC, reviewing VN, supervision.

Declarations

Conflict of interest The authors state that there is no conflict of interest.

References

Abd El-Naby HH, Dawood YH (2008) Natural attenuation of uranium and formation of autunite at the expense of apatite within an oxidizing environment, south Eastern Desert of Egypt. Appl Geochem 23:3741–3755

Alexandre P (2010) Mineralogy and geochemistry of the sodium metasomatism-related uranium occurrence of Aricheng South, Guyana. Miner Deposita 45:351–367

Alexandre P, Kyser TK (2005) Effects of cationic substitutions and alteration in uraninite, and implications for the dating of uranium deposits. Can Mineral 43:1005–1017

Andreeva OV, Golovin VA, Petrov VA (2010) Wall-rock argillic alteration and uranium mineralization of the northwestern Strel'tsovka Caldera. Geol Ore Deposits 52:32–45

Bassahak J (1988) Le complexe plutonique de Kogué (poli. nord Cameroon). Pétrologie-Géochimie-Pétrologie Structurale; sa place dans la Chaine panafricaine au Nord Cameroon." Thèse de Doctorat, Université de Nancy I, 259p

Bau M (1996) Controls on the fractionation of isovalent trace elements in magmatic and aqueous systems: evidence from Y/Ho, Zr/Hf, and lanthanide tetrad effect. Contrib Mineral Petrol 123:323–333

Bouchez JL, Delas C, Gleizes G, Nédélec A, Cuney M (1992) Submagmatic microfractures in granites. Geology 20:35–38

Brookins DG (1975) Coffinite-uraninite stability relations in grants mineral belt, New Mexico. Abs Bull Am Assoc Pet Geol 59:90519

Bros R, Hidaka H, Kamei G, Ohnuki T (2003) Mobilization andmechanisms of retardation in the Oklo natural reactor zone 2 (Gabon)-interferences from U, REE, Zr, Mo and Se isotopes. Appl Geochem 18:1807–1824

Broska I, Williams CT, Janak M, Nagy G (2004) Alteration and breakdown of xenotime-(Y) and monazite-(Ce) in granitic rocks of the Western Carpathians, Slovakia. Lithos 82:71–83

Burns PC, Finch R (1999) Uranium: mineralogy, geochemistry and environment. Mineralogical society of America. Rev Mineral 38:255–319

Bute Saleh I, Xiaoyong Y, Suh EC, Girei Bala M, Usman Bappah M (2020) Mineralogy, geochemistry and ore genesis of Kanawa uranium mineralization, Hawal Massif, eastern Nigeria terrane: Implications for uranium prospecting in Nigeria and Cameroon. Ore Geol Rev 120:103381. https://doi.org/10.1016/j.oregeorev.2020.103381

Cavalcanti JAD, Bessa MDMR, Santos RV, Veríssimo CUV, Parente CV (2018) A hydrothermal karst-hosted U-P deposit related to Pangea break-up: Itataia deposit, Borborema province, Northeastern Brazil—a review. J Geol Surv Braz 1(1):43–60

Chambefort I, Kamenetsky V, McPhie J, Bath A, Agangi A, Allen SR, Ehrig K, Green N (2009) The Olympic Dam Cu-Au-U Deposit, South Australia: Was Fluorine a key in forming this Giant? In: Proceedings of the Tenth Biennial SGA Meeting, Townsville, Australia, 207–209

Chappell BW, White AJR (1992) I- and S-type granites in the Lachlan fold belt. Transact R Soc Edinb Earth Sci 83:1–26

Chen YW, Bi XW, Hu RZ, Dong SH (2012) Element geochemistry, mineralogy, geochronology and zircon Hf isotope of the Luxi and Xiazhuang granites in Guangdong province, China: implications for U mineralization. Lithos 150:119–134

Cinelu S, Cuney M (2006) Sodic metasomatism and U-Zr mineralization, a model based on the Kurupung Batholith (Guyana). Geochim Cosmochim Acta 70:18–103

Cuney M (2009) The extreme diversity of uranium deposits. Miner Deposita 44:3–9

Cuney M, Kyser K (2008) Recent and not-so-recent developments in uranium deposits and implications for exploration. Mineralogical Association of Canada Shortcourse Series, Quebec, Volume 39

Cuney M, Emetz A, Mercadier J, Mykchaylov V, Shunko V, Yuslenko A (2012) Uranium deposits associated with Na-metasomatism from central Ukraine: a review of some of the major deposits and genetic contraints. Ore Geol Rev 44:82–106

Dahlkamp FJ (1993) Uranium ore deposits. Springer, Berlin, p 460

Dodge CJ, Francis AJ, Gillow JB, Halada GP, Eng C, Clayton CR (2002) Association of uranium with iron oxides typically formed on corroding steel surfaces. Environ Sci Technol 36:3504–3511

Edwards CR, Oliver AJ (2000) Uranium processing: a review of current methods and technology. J Miner Met Mater Soc 52:12–20

Embui V, Suh EC, Cottle J, Etame J, Mendes J, Agyingi C, Vishiti A, Shemang E, Lehmann B (2019) Zircon chemistry and new laser ablation U–Pb ages for uraniferous granitoids in SW Cameroon. Acta Geochimica 39:43–66

Finch RJ, Ewing RC (1992) The corrosion of uraninite under oxidizing conditions. J Nucl Mater 190:133–156

Finch RJ, Murakami T (1999) Systematics and paragenesis of uranium minerals. In: Burns PC, Finch R (eds) Uranium mineralogy geochemistry and the environment, vol 38. Mineralogical Society of America, Chantilly, pp 91–180 (**Reviews in Mineralogy**)

Fojt B, Dolnicek Z, Kopa D, Sulovsky P, Skoda R (2005) Paragenesis of the hypogene associations from the uranium deposit at Zálesí near Javorník in Rychlebské hory Mts., Czech Republic: In René et al. (2019) Uraninite, Coffinite and Ningyoite from Vein-Type Uranium Deposits of the Bohemian Massif (Central European Variscan Belt). Minerals 9:123. https://doi.org/10.3390/min9020123

Frondel C (1958) Systematic mineralogy of uranium and thorium. US Geol Surv Bull 1064:400

Frondel JW, Fleischer M (1955) Glossary of uranium- and thorium-bearing minerals, 3rd edn. US Geol Surv Bull 1009:169–209

Giére R (1993) Transport and deposition of REE in H_2S-rich fluids: evidence from accessory mineral assemblages. Chem Geol 110:251–268

Goldhaber MB, Hemingway BS, Mohagheghi A, Reynolds RL, Northrop HR (1987) Origin of coffinite in sedimentary rocks by a sequential adsorption-reduction mechanism. Bull Mineral 110:131–144

Grechishnikov MP, Kramar OO, Kuznetsova SV, Makivchuk OF, Nikolayenko VI, Halemus U, Smellie JAT, Wilson MR (1977) Uranium genesis within the Arjeplog–Arvidsjaur–Sorsele uranium province/northern Sweden. IAEA Tec-Doc Rep 361:21–42

Hu RZ, Bi XW, Zhou MF, Peng JT, Su WC, Liu S, Qi HW (2008) Uranium metallogenesis in South China and its relationship to crustal extension during the Cretaceous to tertiary. Econ Geol 103:583–598

Isobe H, Murakami T, Ewing RC (1992) Alteration of uranium minerals in the Koogarra deposit, Australia: unweathered zone. J Nucl Mater 190:174–187

Janeczek J, Ewing RC (1992a) Coffinitization—a mechanism for the alteration of UO_2 under reducing conditions. Mater Res Soc Symp Proc 257:497–504

Janeczek J, Ewing RC (1992b) Dissolution and alteration of uraninite under reducing conditions. J Nucl Mater 190:157–173

Janeczek J, Ewing RC (1995) Mechanisms of lead release from uraninite in the natural fission reactors in Gabon. Cosmochim Acta 59:1917–1931

Kempe U (2003) Precise electron microprobe age determination in altered uraninite: consequences on the intrusion age and the metallogenic significance of the Kirchberg granite (Erzgebirge, Germany). Contrib Miner Petrol 145:107–118

Kotzer TG, Kyser TK (1993) U and Pb isotopic and chemical variations in uraninite: implications for determining the temporal and fluid history of ancient terranes. Am Mineral 78:1262–1274

Kouske AP (2013) Uranium occurrences associated with sodium metasomatism within the Pan-African mobile zone - the Kitongo, Salaki and Mayo Nielse uranium mineralizations in the Poli region, northern Cameroon: structural, petrographic and geochemical investigations, PhD dissertation thesis, University of Yaoundé I (Cameroon), Department of Earth Science, Applied Geology-Metallogeny 300 p

Kouske AP, Cheo ES, Ghogomu RT, Ngako V (2012) Na-metasomatism and uranium mineralization during a two-stage albitization at Kitongo, northern Cameroon: structural and geochemical evidence. Int J Geosci 3:258–279
Kribek B, Zak K, Dobes P, Leichmann J, Pudilova M, René M, Scharm B, Scharmova M, Hajek A, Holeczy D, Hein UF, Lehmann B (2009) The Rozna uranium deposit (Bohemian Massif, Czech Republic): shear zone-hosted, late Variscan and post-Variscan hydrothermal mineralization. Miner Deposita 44:99–128
Le Fur Y (1971) Les indices de Cuivre du Groupe Volcano Sédimentaire de Poli (Cameroun). Bulletin Du BRGM 6:79–91
Leroy J, Holliger P (1984) Mineralogical, chemical and isotopic (U–Pb method) studies of Hercynian uraniferous mineralizations (Margnac and Fanay mines, Limousin, France). Chem Geol 45:121–134
Maruejol, P., (1989) Les albitites uraniferes de Kitongo (Nord- Cameroun). Let. Inf. du CREGU, 40
Migdisov A (2009) The solubility of Zr in F-bearing hydrothermal solutions. Geochim Cosmochim Acta 73:A879
Missana T, Maffiotte U, García-Gutiérrez M (2003) Surface reactions kinetics between nanocrystalline magnetite and uranyl. J Colloid Interface Sci 261:154–160
Mosoh Bambi CM, Suh EC, Nzenti JP, Frimmel H (2012) U Mo mineralization potential in Pan-African granites, southwestern Cameroon: economic geology of the Ekomédion prospect. J Afr Earth Sc 65:25–45
Mosoh Bambi CK, Frimmel HE, Zeh A, Suh CE (2013) Age and origin of Pan-African granites and associated U–Mo mineralization at Ekomédion, southwestern Cameroon. J Afr Earth Sci 88:15–37
Ngako V (1999) Les Déformations continentales panafricaines en Afrique Centrale. Université de Yaoundé I, Cameroun, Résultat d'un poinçonnement de type himalayen. Thèse de Doctorat d'Etat, p 301p
Ngako V, Njonfang E (2011) Plates amalgamation and plate destruction, the Western Gondwana history. In: D. Closson (Ed.), Tectonics. INTECH, UK 3–34
Ngako V, Affaton P, Njonfang E (2008) Pan-African tectonics in northwestern Cameroon: implications for the history of western Gondwana. Gondwana Res 14:509–522
Njel UO (1986) Paléogéographie d'un Segment de l'Orogenèse Panafricaine, la Ceinture Volcano-Sédimentaire de Poli (Nord Cameroun). Compte Rendu De L'académie Des Sciences 30:1737–1742
Norberg N, Harlov D, Neusser G, Wirth R, Rhede D, Morales L (2013) Experimental development of patch perthite from synthetic cryptoerthite: microstructural evolution and chemical re-equilibration. Am Minerol 98:1429–1441
Oesterlen M, Vetter U (1986) Petrographic-geochemical caracteristics andgenesis of an albitized uraniferous granite innorthern Cameroon, Africa. Vein type uranium deposits, I.A.E.A. -TEC-DOC-361: 113–142
Parsons I, Lee MR (2009) Mutual replacement reactions in alkali feldspars I: microtexures and mechanisms. Contrib Mineral Petrol 157:641–666
Penaye J (1988) Pétrologie et structure des ensembles métamorphiques au Sud-Est de Poli (Nord–Cameroun). Rôles respectifs du socle protérozoïque inférieur et de l'accrétion crustale Pan-Africaine. Thèse Doctorat de l'INPL, 196p
Penaye J, Kröner A, Toteu SF, Van Schmus WR, Doumnang JC (2006) Evolution of the Mayo Kebbi region as revealed by zircon dating: an early (ca. 740 Ma) Pan-African magmatic arc in southwestern Chad. J Afr Earth Sc 44:530–542
Phillips ER (1980a) Myrmekite as a marker between pre-aqueous and post aqueous phase saturation in granitic systems: discussion. Geol Soc Am Bull 91:672–674
Phillips ER (1980b) On polygenetic myrmekite. Geol Mag 117:29–36
Pinna P, Calvez JY, Abessolo A, Angel JM, Mekoulou-Mekoulou T, Mananga G, Vernhet Y (1994) Neo-proterozoic events in the Tcholliré area, Pan african crustal growth and geodynamics in central-northern Cameroon (Adamawa and North Provinces). J Afr Earth Sc 18:347–353
Pointer VM, Asworth JR, Simpson PR (1989) Genesis of coffinite and the U–Ti association in lower Old Red sandstone sediments, Ousdale, Caithness. Scotland Miner Deposita 24:117–123
Polito PA, Kyser TK, Stanley C (2009) The Proterozoic, albitite-hosted, Valhalla uranium deposit, Queensland, Australia: a description of the alteration assemblage associated with uranium mineralizationin diamond drill hole V39. Miner Deposita 44:11–40
Pownceby MI, Johnson C (2013) Geometallurgy of Australian uranium deposits. Ore Geol Rev 56:25–44
Ram R, Charalambous FA, McMaster S, Pownceby MI, Tardio J, Bhargava SK (2013) Chemical and micro-structural characterisation studies on natural uraninite and associated gangue minerals. Miner Eng 45:159–169
René M (2017) Alteration of granitoids and crystalline rocks and uranium mineralizationin the Bor pluton area, Bohemian Massif, Czech Republic. Ore Geology Review 81:188–200
René M, Dolnicek Z (2017) Uraninite, coffinite and brannerite from shear-zone hosted uranium deposits of the Bohemian Massif (Central European Variscan belt). Minerals 7:50. https://doi.org/10.3390/min7040050
René M, Dolnicek Z, Sejkora J, Skacha P, Srein V (2019) Uraninite, coffinite and Ningyoite from vein-type uranium deposits of the bohemian massif (central European Variscan Belt). Minerals. https://doi.org/10.3390/min9020123
Rubin JN, Henry CD, Price JG (1993) The mobility of zirconium and other"immobile" elements during hydrothermal alteration. Chem Geol 110:29–47
Savary V, Pagel M (1997) The effects of water radiolysis on local redox conditions in the Oklo, Gabon natural fission reactors 10 and 16. Geochim Cosmochim Acta 61:4479–4494
Scott T, Allen GC, Heard PJ, Randell MG (2005) Reduction of U(VI) to U(IV) on the surface of magnetite. Geochimica et Cosmochimica Acta 69:5639–5646
Singer DM, Chatman SM, Ilton ES, Rosso KM, Banfield JF, Waychunas GA (2012) Identification of simultaneous U(VI) sorption complexes and U(IV) nanoprecipitates on the magnetite (111) surface. Environ Sci Technol 46:3811–3820
Skomurski FN, Ilton ES, Engelhard MH, Arey BW, Rosso KM (2011) Heterogeneous reduction of U^{6+} by structural Fe^{2+} from theory and experiment. Geochim Et Cosmochim Acta 75:7277–7290
Smith DK (1984) Uranium mineralogy. In: de Vivo B, Ippolito F, Capaldi G, Simpson PR (eds) Uranium geochemistry, mineralogy, geology, exploration and resources. The Institution of Mining and Metallurgy, London, pp 43–88
Suh CE, Dada SS (1998) Mesostructural and Microstructural Evidences for a Two Stage Tectono-Metallogenetic Model for the Uranium Deposit at Mika, Northeastern Nigeria: A Research note Nonrenewable Resources 7(1).
Toteu SF (1990) Geochemical characterization of the main petrographical and structural units of northern Cameroon: implications for the Pan-African evolution. J Afr Earth Sc 10:615–624
Toteu SF, Dumont JF, Bassahak J, Penaye J (1984) Complexe de Base et Séries Intermediaires Dans la Zone Mobile Panafricaine de Poli au Cameroon. Comptes Rendus De L'académies Des Sciences 299:561–564
Toteu SF, Michard A, Bertrand JM, Rocci G (1987) U/Pb of Precambrian rock from North-Cameroon. Orogenic evolution and chronology of the Pan-African belt of central Africa. Precambr Res 37:71–87
Toteu SF, Van Schmus RW, Penaye J, Michard A (2001) New U-Pb and Sm-Nd data from north central Cameroon and its bearing on the Pre-Pan-African history of Central Africa. Precambrian Res 108:45–73
Toteu SF, Penaye J, Deloule E, Van Schmus WR, Tchameni R (2006) Diachronous evolution of Volcano—sedimentary Basins north of

the Congo Craton, insights from U–Pb ion microprobe dating of zircons from the Poli, Lom and Yaounde´ groups (Cameroon). J Afr Earth Sc 44:428–442
Vanderhaeghe O, Anne-Sylvie AM, Mbaguedje D, Eglinger A, Ohnenstetter M, Isseini M, Cuney M, Poujol M, Van Lichtervelde M (2020) Uranium mineralization associated with late magmatic ductile to brittle deformation and Na–Ca metasomatism of the Pan-African A-type Zabili syntectonic pluton (Mayo-Kebbi massif, SW Chad). Mineralium Deposita. https://doi.org/10.1007/s00126-020-00999-1
Verissimo CUV, Santos RV, Parente CV, de Oliveira CG, Cavalcanti JAD, Neto JDAN (2016) The Itataia phosphate-uranium deposit (Ceara, Brazil) new petrographic, geochemistry and isotope studies. J South Am Earth Sci 70:115–144
Wilde AR, Mernagh TP, Bloom MS, Hoffmann CF (1989) Fluid inclusion evidence on the origin of some Australian unconformity-related uranium deposits. Econ Geol 84:1627–1642
Zacharias J, Adamovic J, Konecny P (2008) The uraninite pyrite association, a sensitive indicator of changes in paleofluid composition: an example from the Ohre (Eger) Graben, Bohemian Massif, Czech Republic. Can Mineral 46(5):1159–1172

Authors and Affiliations

Arnaud Patrice Kouske[1] · Martine Gerard[2] · Jacques Etame[3] · Ngouo Sylvestre Kanouo[4] · Milan Stafford Tchouatcha[5] · Tanwi Richard Ghogomu[6] · Michel Cuney[7] · Suh Emmanuel Cheo[8] · Vincent Ngako[9]

Martine Gerard
martine_gerard@hotmail.fr

Jacques Etame
etame.jacques@yahoo.fr

Ngouo Sylvestre Kanouo
sylvestrekanouo@yahoo.fr

Milan Stafford Tchouatcha
inter_milanac@yahoo.fr

Tanwi Richard Ghogomu
rtghogomu@yahoo.com

Michel Cuney
michel.cuney@univ-lorraine.fr

Suh Emmanuel Cheo
chuhma@yahoo.com

Vincent Ngako
vincentn@yahoo.fr

[1] Department of Civil Engineering, The University Institute of Technology, University of Douala, Douala, Cameroon

[2] Institut de minéralogie, de physique des matériaux et de cosmochimie UPMC, Université de Paris VI, Paris, France

[3] Department of Earth Sciences, University of Douala, Douala, Cameroon

[4] Mineral Exploration and Ore Genesis Unit, Department of Mines and Quarries, Faculty of Mines and Petroleum Industries, University of Maroua, 46, Maroua, Cameroon

[5] Department of Earth Sciences, University of Dschang, P.O. Box 67, Dschang, Cameroon

[6] Department of Security, Quality and Environment, Faculty of Mines and Petroleum Industries, University of Maroua, 46, Maroua, Cameroon

[7] Université de Lorraine, CREGU, CNRS, GeoRessources, Boulevard des Aiguillettes, P.O. Box B.P. 70239, 54506 Vandoeuvre-lès-Nancy, France

[8] Economic Geology Unit, Department of Geology, University of Buea, P.O. Box 63, Buea, Cameroon

[9] Institute for Geological and Mining Research (IGMR) Yaoundé, P.O. Box B.P. 4110, Yaoundé, Cameroon